


## Article

# The base metal sulfide and Ni–Co arsenide-bearing veins of Valsassina, Lombardy, Italy: a preliminary study

## Mineralogy, petrology and geochemistry of pegmatites: Alessandro Guastoni memorial issue

Fabrizio Vergani<sup>1</sup>, Marilena Moroni<sup>2</sup>, Paolo Gentile<sup>3</sup> and G. Diego Gatta<sup>2</sup> 

<sup>1</sup>Dipartimento di Scienze dell'Ambiente e della Terra "DISAT", Università degli Studi di Milano Bicocca, Piazza della Scienza 4, 26100 Milano; <sup>2</sup>Dipartimento di Scienze della Terra "A. Desio", Università degli Studi di Milano, Via Botticelli 23, 20133 Milano; and <sup>3</sup>U.O. Piattaforma di Microscopia, Università degli Studi di Milano Bicocca, Piazza della Scienza 4, 26100 Milano

### Abstract

Valsassina (Lombardy, Northern Italy) is located in the Lombard Southern Alps and is characterised by the presence of a metamorphic basement, by a major late Variscan intrusive complex and by Carboniferous–Permian volcano-sedimentary cover units. These rocks host a pervasive system of inadequately studied mineralised veins. These veins are characterised by base metal (Pb, Zn, Cu and Fe) and complex polymetallic assemblages.

In this study, we have investigated the ore textures, mineral compositions of sulfides and sulfosalts (by EMPA–WDS and LA–ICP–MS analyses), and stable isotopes (C and O) in carbonate gangue minerals of various mineralised veins to determine the conditions of deposition of these ore deposits. Two different vein families can be recognised in Valsassina: NNW–SSE veins characterised by a complex polymetallic sulfide–sulfosalt assemblage, also with Ni–Co–Fe arsenides and other Ag–Bi-bearing minerals; and NE–SW veins with a simpler, base metal sulfide assemblage. The Ni–Co-bearing NNW–SSE veins have some distinctive features of the 'five-element vein' type deposits, with the Ni–Co–Fe arsenide ore stage pre-dating a sulfide-tetrahedrite-dominated ore stage. LA–ICP–MS data for pyrite and sphalerite, and stable isotopic compositions (C and O) of the carbonate gangue minerals, show no clear differences between the two families of veins, which are probably linked genetically. The isotopic compositions of the Valsassina vein carbonates are closely comparable with the signature of several major five-element ore districts. Preliminary temperature estimates for the Valsassina vein systems were based on the sphalerite composition, applying the GGIMFis geothermometer. The estimated temperatures for the sulfide-dominated ore stage post-dating the Ni–Co minerals precipitation range between 100 and 250°C. The crosscutting relationships, observed for all the veins with the host rocks, suggest a possible late to post Variscan (late Permian) age, making these vein systems comparable with other late–post Variscan polyphase hydrothermal events affecting large sectors of the Southern Alpine domain.

**Keywords:** Valsassina; ore deposits; base metal sulfides; Ni–Co arsenides; five-element veins; EMPA-WDS; LA–ICP–MS; C–O stable isotopes; pyrite; sphalerite

(Received 21 October 2023; accepted 14 January 2024; Accepted Manuscript published online: 22 January 2024; Guest Editor: Fabrizio Nestola)

### Introduction

Located in the western end of the Orobic domain of the Southern Alpine belt (Lombardy, Northern Italy, [Fig. 1](#)), Valsassina represents a historically important mining area exploited since the Middle Ages (and probably before), especially for iron, lead, copper, silver and baryte. The valleys of Valsassina are host to various types of mineralisation including Mississippi Valley Type (MVT) deposits in Triassic limestone units (Rodeghiero *et al.*, 1986;

Vergani, 2022). There, swarms of hydrothermal veins comprising base metal (Pb, Zn, Cu, Fe) and complex polymetallic assemblages occur in a variety of rock types ranging from Palaeozoic metamorphic basement to Variscan intrusive rocks and Permo-Carboniferous volcano-sedimentary units.

None of these vein systems has previously been studied in detail, either in terms of geological setting, or mineralogical and geochemical features, although a spatial relationship with the Variscan Val Biandino intrusive complex (Di Colbataldo, 1967; Crippa, 2017) might suggest a possible link to its hydrothermal circuit (Di Colbataldo, 1967).

The Lombard Southern Alps host several late Variscan ore deposits, mainly linked to magmatic–volcanic activity or to regional-scale hydrothermal systems. These deposits were

**Corresponding author:** G. Diego Gatta; Email: [diego.gatta@unimi.it](mailto:diego.gatta@unimi.it)

This paper is part of a thematic set on pegmatites in memory of Alessandro Guastoni  
**Cite this article:** Vergani F., Moroni M., Gentile P. and Gatta G.D. (2024) The base metal sulfide and Ni–Co arsenide-bearing veins of Valsassina, Lombardy, Italy: a preliminary study. *Mineralogical Magazine* 1–26. <https://doi.org/10.1180/mgm.2024.3>

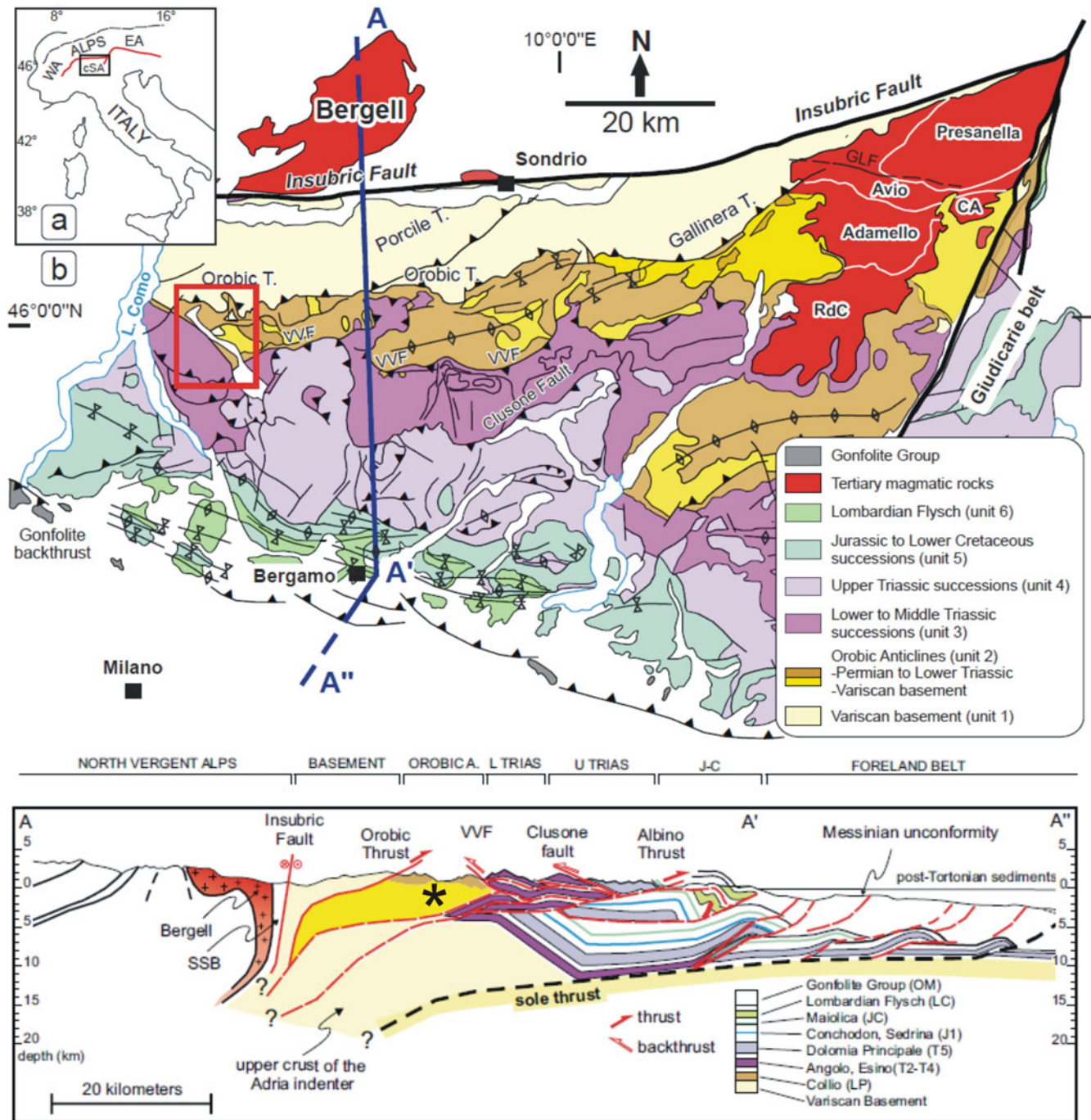


**Figure 1.** Geological sketch map of the South-alpine domain in Lombardy. The Valsassina Valley area is located in the red rectangle. This valley is characterised by two main geological areas, separated by the Valtorta Fault (VF). In the section, the black asterisk indicates the Orobic Basement. Reproduced from Zanchetta *et al.* (2015).

exploited over the centuries, playing a key role in the Lombard economy which could extend to the present, as evidenced by the large unexploited U deposits of Novazza and Val Vedello (Cadel *et al.*, 1986). In addition, in the last few years, a series of new studies about the late Variscan hydrothermalism of Lombard Southern Alps have been published (e.g. Servida *et al.*, 2010; Martin *et al.*, 2017; Locchi *et al.*, 2022; Zanchetta *et al.*, 2022), underlining a renewed scientific interest in these deposits.

Based on preliminary observations (Bianchi, 1999; Vergani, 2019), this study represents a new contribution towards a

thorough characterisation of the vein-type ore deposits of the Valsassina district. Geological features of the mineralisation are reported, together with the paragenetic reconstruction of the primary mineral assemblages based on data acquired using optical microscopy, electron microprobe analysis in wavelength-dispersion spectroscopy mode (EMPA-WDS), laser ablation inductively coupled plasma mass spectrometry (LA-ICP-MS) and stable isotope analyses of C and O. The present investigations on the primary vein assemblages aim to provide a potential genetic model for this mineralisation. Their characterisation can

eventually provide new insights for a better understanding of the hydrothermal events, which have distinguished the Southern Alps and their connection to the late–post Variscan geodynamic.

## Geological background

### Geological framework of Valsassina

Valsassina is located to the NE of the town of Lecco. Valsassina is bordered by the Grigna massif, to the West, and the margin of the Orobic Alps, to the East.

The region is divided into two main structural domains by an important regional structure: the Valtorta Fault (see Fig. 2), a major transcurrent fault interpreted as being of Alpine age (Laubscher, 1985; Berra and Siletto, 2006). The northern domain consists of metamorphic rocks of the South Alpine basement, the Val Biandino and Valle San Biagio intrusive complexes, Carboniferous to Permian volcano–sedimentary cover rocks, and finally Mesozoic carbonate rocks separated from the underlying Palaeozoic rocks by the Northern Grigna thrust fault system (Fig. 2). The southern domain consists mainly of Mesozoic carbonate rocks.

The South Alpine basement crops out in the core of a big regional fold structure, the Orobic Anticline. The basement consists predominantly of Carboniferous paragneiss and quartz micaschists (315–350 Ma), with rare kyanite relics, interpreted as products of prograde Barrovian metamorphism, followed by retrocession to greenschist facies (Siletto *et al.*, 1993). In the Orobic basement, metabasites and graphite schist levels also occur (De Sitter and De Sitter-Koomans, 1949; Cadel *et al.*, 1996). In the Valsassina area, the Carboniferous–Permian

volcano–sedimentary cover is represented by volcanic and continental clastic rock units of the Monte Cabianca Formation, Pizzo del Diavolo Formation and polymictic Ponteranica Conglomerate (Collio domain), followed by conglomerates and sandstones of the Verrucano Lombardo Formation that sealed, locally with angular unconformity, the complex stratigraphy of the Permian tectonic basins (Berra *et al.*, 2016 and references therein). The intrusive complexes emplaced in the basement north of the Valtorta fault are the so-called Val Biandino quartz–diorite and the minor body of the Valle San Biagio Granite, the latter interpreted as a hypo-abysal apophysis of the major Val Biandino intrusion (Crippa, 2017)(Fig. 2). The intrusive mass of Val Biandino emerges at the nucleus of the Orobic Anticline, precisely in the culmination of Valsassina and Valtorta Valley. The intrusion is formed by two main stocks and by a series of lenticular masses and numerous leucogranitic, aplitic and pegmatitic bodies (Pasquarè, 1967; De Capitani, 1982; De Capitani and Liborio, 1988) (Fig. 2). The Val Biandino pluton is characterised by a pronounced lithological variability, with dominant biotite-bearing quartz–diorites (rich in mafic xenoliths) associated with tonalite and rarer gabbro–diorites and norites (e.g. one of the major lenticular outcrops north of Introbio). The pluton has a calc-alkaline affinity, with a ‘bimodal’ character of magmatism (De Capitani, 1982; De Capitani and Liborio, 1988). The Valle San Biagio Granite delimits the intrusive complex of Val Biandino to the West (Fig. 2). This intrusive body is composed of porphyritic leucogranites, occasionally with granophyric textures. The exposed contacts between the Valle San Biagio Granite and the Val Biandino plutons are always tectonic, underlined by tourmaline-bearing cataclasites (Sciunnach, 2001). In large sectors of Valsassina, the basement schists show

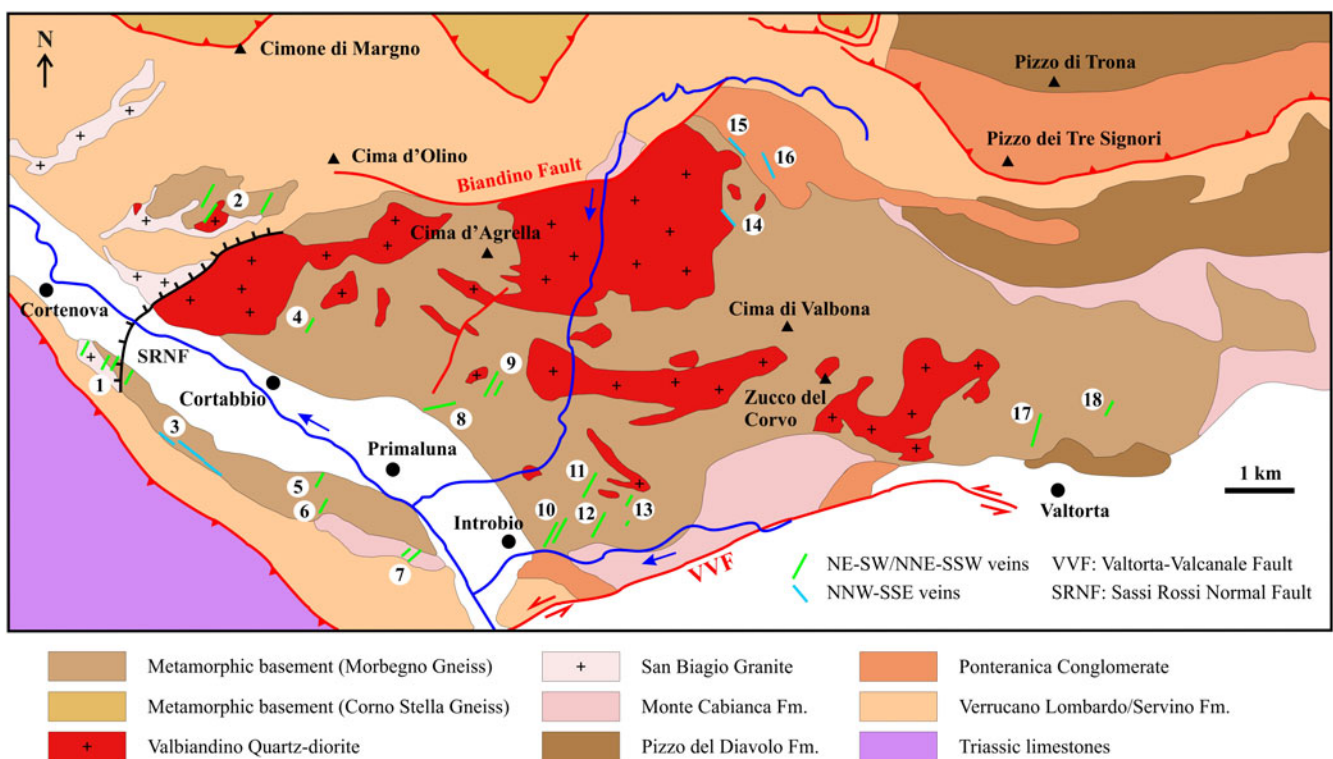


**Figure 2.** Simplified geological map showing the main lithologies, the position of the intrusive masses and the principal mining areas of Valsassina. Most of the orebodies are hosted inside the metamorphic basement or in proximity of the contacts with the intrusive masses, whereas the Camisolo and Pra Piazze lodes are hosted by Permian volcano clastic rocks. 1: Prato San Pietro, 2: Val Rossiga, 3: Cortabbio, 4: Valle della Fusa, 5: Valle di Contra, 6: Alpe Piattedo, 7: Pra Piazze, 8: Valle delle Noci, 9: Falpiano, 10: Introbio, 11: Ombrega, 12: Corno, 13: Zucco dell'Orso, 14: Valbona, 15: Cobbio, 16: Camisolo, 17: Costa Alta-Frer, 18: Monte Pigolotta.

widespread and sometimes extensive (up to 400 m large) signs of thermo-metamorphism, suggesting that these intrusive bodies are mainly sub-outcrops (see also Gaetani *et al.*, 2012). A recent SHRIMP U–Pb study reported a zircon radiometric age of  $289 \pm 0.8$  Ma for the Val Biandino pluton and of  $284.5 \pm 1.0$  Ma for the Valle San Biagio Granite (Crippa, 2017). Therefore, the intrusion ages of Val Biandino and Valle San Biagio are coeval with the volcanic rocks of the Monte Cabianca Formation. (Cadel, 1986), which might represent their effusive analogue (Froitzheim *et al.*, 2008).

### The Valsassina hydrothermal system

The hydrothermal vein deposits considered in this investigation occur in the central part of Valsassina. These deposits are hosted in a network of fractures with NE–SW/NNE–SSW and NNW–SSE orientations. Mineralisation occurs mostly as vertical or sub-vertical lodes emplaced within metamorphic basement rocks and near the thermo-metamorphic contact halo of the Valbiandino intrusive (Di Colbertaldo, 1967). Some veins (e.g. Prato San Pietro) crosscut the intrusive masses (Di Colbertaldo, 1967; Tizzoni, 1998), whereas others (e.g. Camisolo, Fig. 2) intersect the local Permian volcano–sedimentary sequence.

The thickness of the veins ranges from a few metres up to over ten metres, with a strike extension that can reach over 1 km. The veins consist mainly of base metal sulfides, such as galena, sphalerite, chalcopyrite and pyrite, together with minor arsenopyrite, bournonite and tetrahedrite, associated with quartz–baryte–carbonate gangue (Di Colbertaldo, 1967; Tizzoni, 1998; Bianchi, 1999) (Figs 3, 4). Ag-, Bi- and Ni–Co-bearing minerals also occur in some deposits (Artini, 1903; Guastoni *et al.*, 2015; Guastoni *et al.* 2016a; Guastoni *et al.* 2016b; Bianchi, 1999) (Fig. 4).

The networks of faults that host the veins are considered as late Palaeozoic extensional fracture systems, preserved from subsequent reactivation during the Alpine orogeny (Sciunnach, 2001; Pohl *et al.*, 2018) in analogy to what is observed in other parts of the Orobic basement to the East (e.g. Cadel *et al.*, 1996).

### Sampling and analytical methods

The Valsassina vein system was investigated at ten localities with ancient mine workings (Table 1): Camisolo, Cobbio, Cortabbio (Sassi Rossi, Faidallo and Faedo mines), Valbona, Ceppo, Valle di Contra, Piattedo, Pra Piazzo, Val Rossiga and Valtorta (Frer and Costa Alta mines) (Figs 2, 3). Another five sites were preliminarily investigated by field inspections only: Corno, Ombrega, Falpiano, Pessina-Valle delle Noci and Prato San Pietro mines. Forty three samples were collected from mineralised outcrops exposed in trenches and open pits, accessible mine works and mine dumps (Fig. 3). The sampling strategy was planned on the basis of field observations and indicated the most representative deposits, where specimens suitable for the petrographic observations and/or the analytical studies could be collected. Samples for petrographic observations and preparation of polished sections for EMPA–WDS and LA–ICP–MS were collected in the Valbona, Cortabbio and Camisolo mining areas (NNW–SSE veins), as well as in the Valle di Contra, Val Rossiga and Valtorta areas (NE–SW veins).

After mineralogical and microtextural characterisation by optical microscopy, quantitative compositional data for the major and accessory ore minerals were acquired by EMPA–WDS and LA–ICP–MS. Ore petrography and microtextural observations were undertaken by optical and scanning electron

microscopy on polished sections with the same sections being used for EMPA–WDS and LA–ICP–MS micro-chemical analyses of the major and accessory ore minerals, together with additional micro-textural investigations.

A list of the localities and samples studied is in Table 1.

### Optical and SEM petrographic observations

Representative samples taken from dumps, mineralised outcrops and accessible mining galleries were prepared for the reflected light optical microscopy and scanning electron microscopy (SEM) observations. The samples were initially embedded in a two-component epoxy resin (Araldite©) and subsequently cut and polished using silicon carbide grinding disks and 0.3 µm corundum dust.

The prepared samples were observed using a Zeiss Axioscope combined transmitted/reflected light optical microscope equipped with a digital camera. The use of the SEM with energy-dispersive X-ray spectroscopy aided in identifying phases that could not be distinguished clearly by optical observations. SEM investigations were performed with a Tescan VEGA TS 5136XM equipped with an EDAX Genesis 4000 energy-dispersive system (EDS). The samples were positioned on aluminium stubs carrying bi-adhesive carbon pads and successively carbon coated (20 nm), in order to increase sample conductivity.

### EMPA–WDS

Quantitative compositional analyses in wavelength dispersive mode of tetrahedrite, Ni–Co arsenide/sulfarsenides, Bi–Pb sulfides and arsenopyrite were performed using a JEOL JXA – 8200 electron probe equipped with five wavelength-dispersive spectrometers at the UNITECH COSPECT – University of Milan. The analytical conditions for the electron beam were: accelerating voltage 15 kV; beam current 5 nA; beam diameter 1–2 µm; and counting time for each element of 30 s on peak and 10 s on background. Elemental concentrations were determined after applying the  $\varphi(\rho z)$  algorithm and corrections for X-ray fluorescence, absorption, atomic number ( $Z$ ) and matrix effects. Calibration for each element was done using the following standards, for which spectral lines, analysing crystals and detection limits, in ppm, are given in brackets: Zn (pure Zn,  $K\alpha$ , LIFH, 650), Fe (fayalite,  $K\alpha$ , LIFH, 330), Cd (pure Cd,  $L\alpha$ , PET, 280), Cu (pure Cu,  $K\alpha$ , LIFH, 550), Ag (pure Ag,  $L\alpha$ , PET, 260), Ni (nickeline,  $K\alpha$ , LIFH, 350), Co (pure Co,  $K\alpha$ , LIFH, 350), Ge (pure Ge,  $L\alpha$ , TAP, 230), Pb (galena,  $M\alpha$ , PET, 450), Bi (pure Bi,  $M\alpha$ , PET, 330), Sb (pure Sb,  $L\alpha$ , TAP, 450), As (nickeline,  $L\alpha$ , TAP, 200) and S (pyrite,  $K\alpha$ , PET, 100). Back-scattered electron (BSE) images were also collected.

Quantitative compositional WDS analyses of sphalerite and pyrite were performed using a Gemini 500 HR-FEG-SEM equipped with a Bruker parallel beam Quantax wavelength-dispersive spectrometer at the PMIB – Milano Bicocca University. The analytical conditions for the electron beam were: accelerating voltage 15 kV; beam current 10 nA; beam diameter 1–2 µm and counting time for each element of 60 s on peak and 30 s on background. The same analysed spots on sphalerite and pyrite were selected for the LA–ICP–MS analyses. The elements analysed were: Zn (Fe-bearing sphalerite standard;  $L\alpha$  line, TAP crystal, 500 ppm d.l.); Fe (pyrite standard,  $L\alpha$  line, BRML30 crystal, 400 ppm d.l.); and S (pyrite standard,  $K\alpha$  line, PET crystal, 500 ppm d.l.).

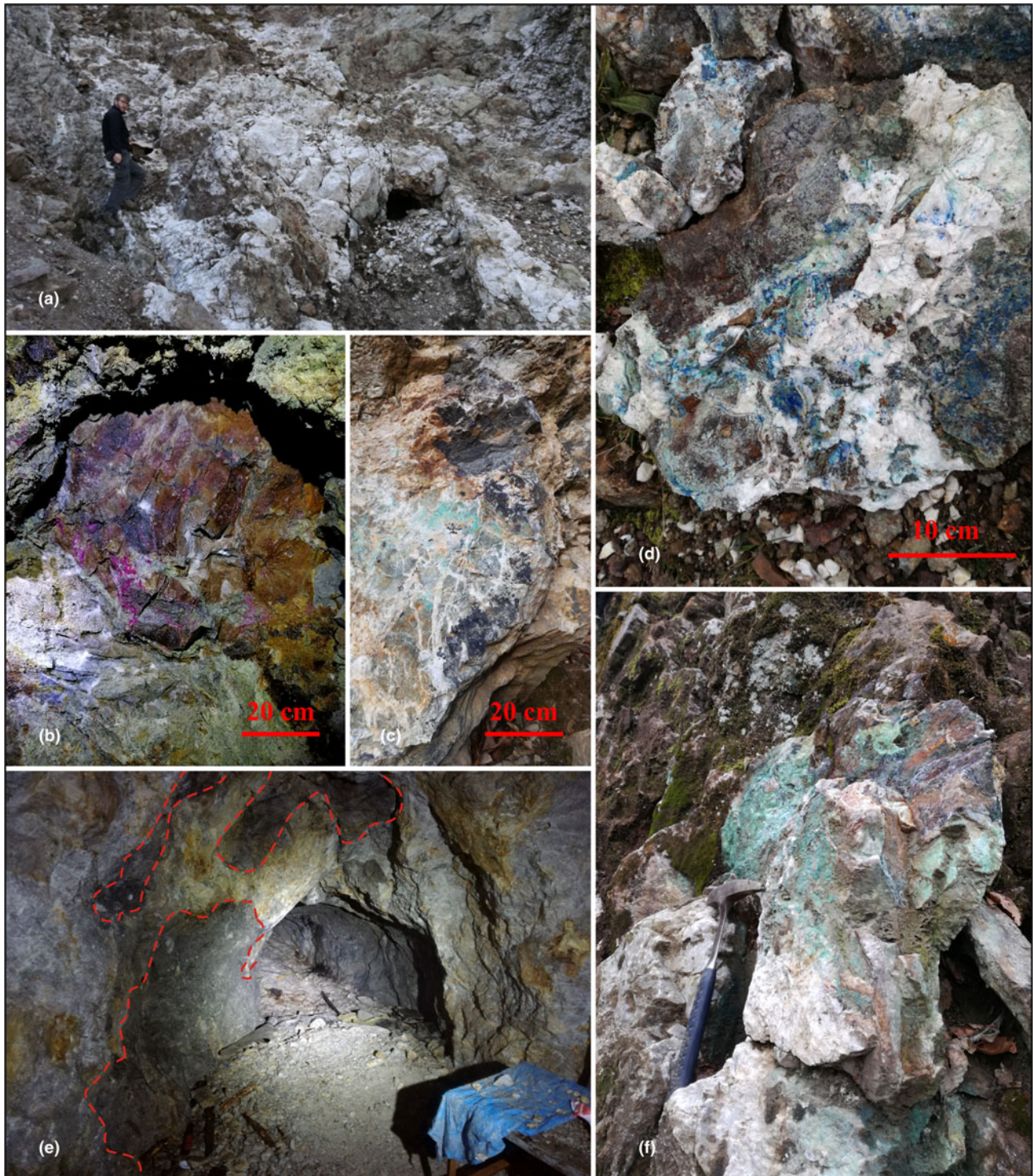


**Figure 3.** Field configurations of the mineralisation in the veins of the Valsassina mining district: (a) outcrop of the big Camisolo lode in the northern part of the mining area, between Santa Barbara and Lina levels; (b) Ni-Co mineralisation in carbonate gangue, with minor Co-bearing secondary phases (Cortabbio mines); (c) stockwork quartz veinlets associated with a broad malachite crust (Valtorta lode); (d) baryte vein up to 20 cm in thickness, hosted in volcanic rocks, that includes several host-rock fragments and that is covered by diverse Cu minerals resulting from tetrahedrite oxidation (Camisolo mine area); (e) view of the mineralisation in the deeper part of the Pra Piazza mine, where the lode consists mainly of quartz and dolomite with minor galena (white and yellowish part of the rocks, outlined by the red dotted line); (f) Cortabbio mine open works, contact between the chalcopyrite-bearing baryte ore body and the host schists.

#### LA-ICP-MS analyses

A wide range of trace elements in pyrite and sphalerite were analysed using LA-ICP-MS at the GeoResources laboratory (Vandoeuvre-lès-Nancy, France), using a 193 nm MicroLas Pro

ArF Excimer coupled with a Agilent 7900 quadrupole ICP-MS. Laser ablations were performed with a constant 5 Hz pulse rate and 60  $\mu\text{m}$  spot size, at 6 J laser energy. The ablation duration for background, peaks and washouts was 30, 40 and 20 s,

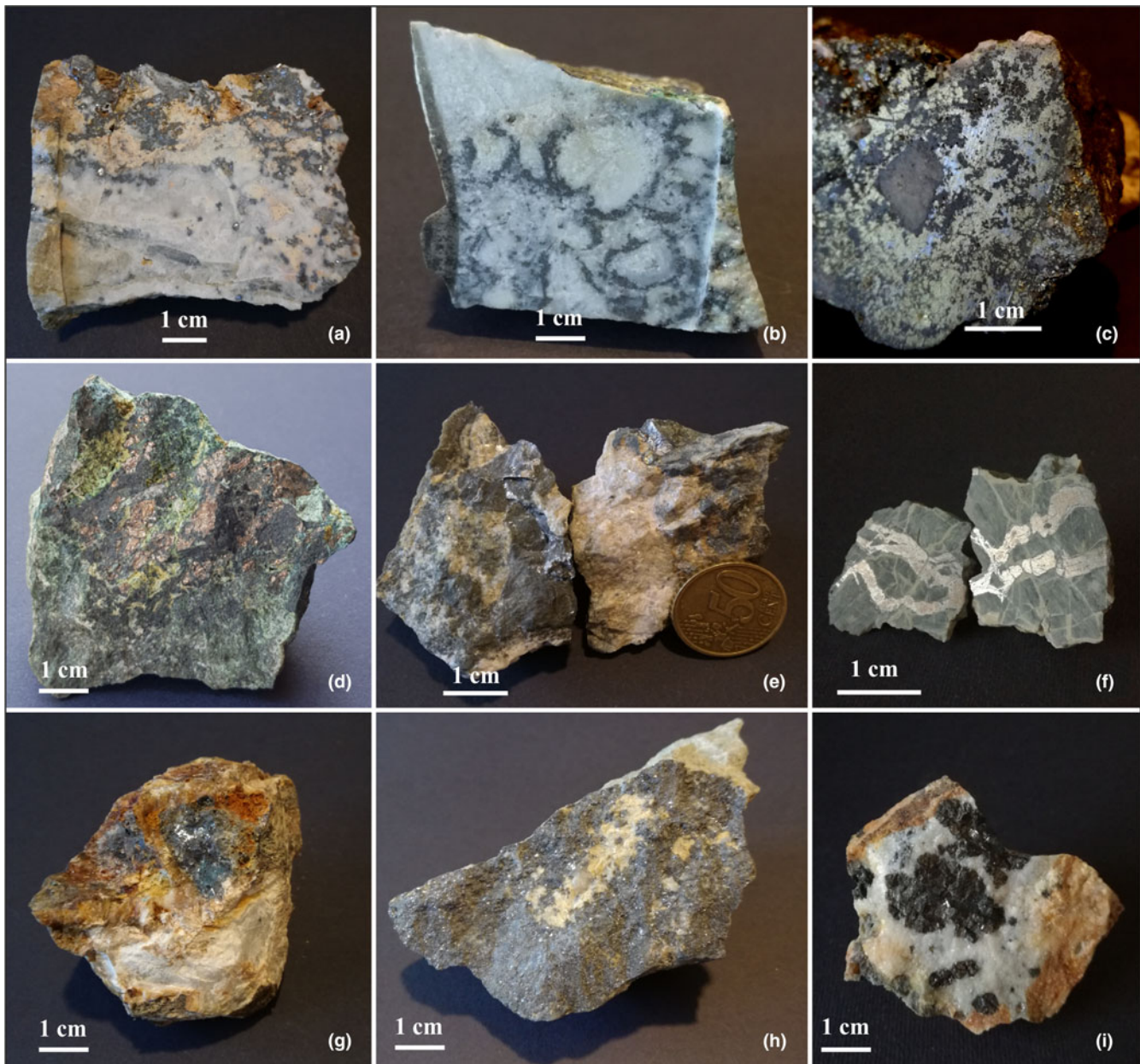


**Figure 4.** Macroscopic textures of the mineralisation in the veins of the Valsassina mining district: (a) galena disseminations within a quartz (white) and siderite (yellowish) gangue, Valbona mine; (b) quartz-rich sample with abundant tetrahedrite from Camisolo mine; (c) detail of a cut semi-massive ore sample from Cortabbio mines, Virginia open pit: chalcopyrite rich with inclusions, apparently of major tetrahedrite s.s.; (d) massive Ni-Co-Fe arsenide nodules with abundant annabergite from Cortabbio mines; (e) nodules of Ni-Co-Fe arsenides sealed in carbonate gangue from Cortabbio mines; (f) Ni-Co-Fe arsenides veins that cross the host schist, associated with hydrothermal carbonate veinlets, Cortabbio mines; (g) galena nodules with limonite (due to siderite and pyrite oxidation) in baryte and (minor) quartz gangue, Ombregia lead prospect; (h) galena-rich sample in carbonate (dolomite) gangue from Pra Piazza mine; (i) dark sphalerite nodules in quartz gangue from Costa Alta mine (Valtorta lode).

respectively. The integration time was 20 ms for all the elements. The ablated material was transported using a constant He flow (650 ml/min) and mixed with Ar in a cyclone coaxial mixer, prior to entering the ICP torch and being ionised. The ions were sampled, accelerated and focused before being separated and analysed in the quadrupole mass spectrometer. The concentrations of the following isotopes were measured:  $^{47}\text{Ti}$ ,  $^{51}\text{V}$ ,  $^{55}\text{Mn}$ ,  $^{57}\text{Fe}$ ,  $^{63}\text{Cu}$ ,  $^{66}\text{Zn}$ ,  $^{59}\text{Co}$ ,  $^{60}\text{Ni}$ ,  $^{71}\text{Ga}$ ,  $^{74}\text{Ge}$ ,  $^{75}\text{As}$ ,  $^{78}\text{Se}$ ,  $^{85}\text{Rb}$ ,  $^{88}\text{Sr}$ ,  $^{89}\text{Y}$ ,  $^{90}\text{Zr}$ ,  $^{93}\text{Nb}$ ,  $^{95}\text{Mo}$ ,  $^{107}\text{Ag}$ ,  $^{111}\text{Cd}$ ,  $^{115}\text{In}$ ,  $^{118}\text{Sn}$ ,  $^{121}\text{Sb}$ ,  $^{125}\text{Te}$ ,  $^{133}\text{Cs}$ ,  $^{137}\text{Ba}$ ,  $^{139}\text{La}$ ,  $^{140}\text{Ce}$ ,  $^{141}\text{Pr}$ ,  $^{146}\text{Nd}$ ,  $^{147}\text{Sm}$ ,  $^{153}\text{Eu}$ ,  $^{157}\text{Gd}$ ,  $^{159}\text{Tb}$ ,

$^{163}\text{Dy}$ ,  $^{165}\text{Ho}$ ,  $^{166}\text{Er}$ ,  $^{169}\text{Tm}$ ,  $^{172}\text{Yb}$ ,  $^{175}\text{Lu}$ ,  $^{178}\text{Hf}$ ,  $^{181}\text{Ta}$ ,  $^{182}\text{W}$ ,  $^{197}\text{Au}$ ,  $^{201}\text{Hg}$ ,  $^{205}\text{Tl}$ ,  $^{208}\text{Pb}$  and  $^{209}\text{Bi}$ . For sphalerite, Mn, Cu, Co, Ni, Ag, Ga, Ge, Se, As, Sb, Mo, Cd, In, Sn, Y, REE and Bi were analysed. For pyrite, V, Cu, Zn, Pb, Co, Ni, Ga, Ge, Se, Sb, As, Hg, Mo, Ag, Te, Au, Tl, Y, REE, Ti, Rb, Sr, Cs, Ba, Hf, Nb and Ta were analysed. The analyses were calibrated with MASS-1 and NIST610 standards. Iron and zinc concentrations of pyrite and sphalerite were used as internal standards, respectively. The limit of detection (LOD) and uncertainty depend on the ablation spot diameter and the element analysed. For each analysis, the

**Table 1.** Summary of the mining sites studied, samples and employed analytical techniques. The label VALB3 represents the cataclastic pyrite–arsenopyrite ore facies/assemblage from the Valbona mine. Abbreviations according to Warr (2021).

Mining site	coordinates (WGS84)	strike	main ore association	gangue	samples	petrographic observations	WDS	LA-ICP-MS	stable isotopes
Camisolo	46.010973, 9.491920	NNW–SSE	Gn, Ttd, Sp ± Ccp	Brt, Qz, Sd	6	CAM1–CAM6	CAM5	CAM5	-
Cobbio	46.014493, 9.483428	NNW–SSE	Gn, Ccp, Ttd, Py ± Apy	Sd, Brt, Qz	3	COB2–COB3	-	-	COB1
Cortabbio	45.983870, 9.405767	NNW–SSE	Ccp, Ttd, Gn, Nc, Rmb, Gdf	Brt, Qz, Sd	10	FD1–FD8	FD3, FD8	FD3	FD9–FD10
Valbona	46.007023, 9.484887	NNW–SSE	Gn, Ttd, Sp, Ccp, Apy, Py	Qz, Sd, Brt	6	VALB1–VALB5	VALB3–4	VALB3–4	VALB6
Val Piana	45.971363, 9.456259	NE–SW	Gn, Sp, Py	Qz, Sd, Brt	3	VP1	-	-	CE2–3
Valle di Contra	45.979203, 9.420055	NE–SW	Gn, Sp ± Ccp	Qz, Sd	3	CO1–CO3	CO1–CO2	CO1	-
Piattedo	45.973879, 9.423952	NE–SW	Gn, Sph	Dol, Qz, Brt	2	PI2	-	-	PI1
Pra Piazza	45.973192, 9.435941	NE–SW	Gn ± Ttd, Ccp, Pyr	Dol, Qz, Brt	5	PP3–5	-	-	PP1–2
Val Rossiga	46.008420, 9.406577	NE–SW	Gn, Sp, Pyr	Qz, Sd, Brt	4	RO2–RO4	RO2	RO2	RO1
Valtorta (Costa Alta)	45.987251, 9.528375	NE–SW	Ccp, Gn, Sp ± Py	Qz, Sd	5	VA1, VA3, VA5	VA3	VA3	VA2, VA4

LOD was calculated using the  $3\sigma$  criterion detailed in Longerich *et al.* (1996), uncertainty was calculated including those on the net transient signal ( $\sigma$ ) and on the internal standard concentration. Minimum LOD were usually lower than 1 ppm for the trace elements analysed at ablation 60  $\mu\text{m}$  spot diameters (see Supplementary Tables S1–2).

### C and O stable isotope analyses

Carbon and oxygen isotopic compositions of the carbonate-bearing samples from the Valsassina veins, coupled with carbonate reference materials, were determined at the Earth Sciences Dept. – University of Milan (ESD-MI). The equipment employed was a ThermoFisher Delta V Isotope Ratio Mass Spectrometer (IRMS), coupled with a Finnigan 2 gas bench. Powders were obtained from 13 carbonate-rich chips. Attempts were made to select carbonate fragments from sulfide-poor portions of the samples, in order to avoid analytical problems. Consequently, special care was taken to remove sulfide crystals, when present, before grinding. A mass of materials ranging between 0.25 mg (pure carbonates) and 0.7 mg (samples with variable fraction of quartz or silicates from wall rock) was used. Carbonate reference materials, i.e. international standards 603, NBS-18 and CO-8 and an internal reference MAMI (Carrara Marble), were employed for monitoring the efficiency of the system and the reproducibility of data. The standards employed were calcite of marine and magmatic origin. The additional reference materials were represented by hydrothermal mineral species similar to those occurring in the samples (siderite and ankerite) and analysed previously by Cortecchi and Frizzo (1993), and at the MLR Key Laboratory of Isotope Geology, Institute of Mineral Deposits in Beijing, China (see Martin *et al.*, 2017). Powders of samples, international standards and internal reference samples were placed into borosilicate vials, sealed with butyl rubber septa, and flushed with  $\text{CO}_2$  at 70°C for 5 minutes for extraction of air. Subsequently, pure anhydrous phosphoric acid was added, and acidification of the powder was performed at 80°C for 12 hours, before the session of isotopic analysis. The high temperature coupled with the small amount of powder ensures a complete dissolution of refractory carbonates and the absence of fractionation due to incomplete reaction of refractory carbonate species before the isotopic analysis. The average  $\delta^{18}\text{O}$  and  $\delta^{13}\text{C}$  values for each sample were derived from a series of ten measurements. The  $\delta^{18}\text{O}$  and  $\delta^{13}\text{C}$  values are reported using the delta ( $\delta$ ) notation in *per mil* (‰), relative to Vienna Pee Dee belemnite (V-PDB) and Vienna standard mean ocean water (V-SMOW), respectively, with precisions of 0.06 to

0.2‰. Data normalisation was performed according to the two-point method described in Paul *et al.* (2007) and comparing each ‘unknown’ sample with both international standards and internal reference material related to the samples.

## Results

### Field observations

According to our field observations (Fig. 3), the Valsassina veins are characterised by two main end-member gangue assemblages, baryte-dominated and quartz-dominated, although a ‘mixed’ quartz–carbonate–baryte assemblage is also recognised. We found that the veins can be divided into two different families based on their directions (Fig. 2): a first set trending in a NNW–SSE direction; and a second set in a NE–SW direction. This difference in the direction of the lodes appears to be associated with some major differences in the vein fillings and in gangue and sulfide assemblages. The second vein set (NE–SW) is characterised by quartz-dominated or mixed gangue, whereas baryte-dominated gangue is only observed in the first vein set (NNW–SSE, e.g. Cortabbio and Camisolo). Interestingly, in the baryte-dominated veins, the metallic minerals often occur as minor components of the vein filling, whereas the quartz-dominated and ‘mixed’ gangue veins often display a higher sulfide abundance coupled with a wide range of sulfide textures from semi-massive to disseminated (Fig. 4). In general, the veins are irregular, with stockwork/braided and ‘pinch-and-swirl’ geometries (with thickness commonly varying abruptly from over one metre to a few centimetres) or truncation by fault planes.

The NNW–SSE vein set (Cortabbio, Camisolo, Valbona and Cobbio lodes) is characterised by a complex mineralisation, here indicated as ‘polymetallic’, consisting of galena, sphalerite and chalcopyrite, accompanied by significant fractions of tennantite–tetrahedrite, arsenopyrite and pyrite, together with bournonite and Ni–Co minerals. At Cortabbio, large masses of sulfides and Ni–Co minerals are always found at the footwall selvage of the baryte-dominated vein. In addition, we found some samples from the Valbona mine dumps containing a particular arsenopyrite–pyrite-rich ore facies, which is unique for the area and has an unknown spatial relation to other paragenetic associations in these lodes.

The second NE–SW vein set (i.e. Ceppo, Valle di Contra, Piattedo, Pra Piazza, Corno, Ombrega, Falpiano, Valtorta, Val Rossiga and Prato San Pietro) is characterised by a simpler paragenesis, dominated by the presence of base metal sulfides like galena, sphalerite and chalcopyrite.

Further descriptions about our field observations of the macroscopic features of mineralisation, textures, etc. are provided in the Supplementary Material (see below).

### Ore petrography

#### *NNW–SSE trending veins ('polymetallic lodes')*

In the Cortabbio, Camisolo and Valbona lodes, the ore phases are semi-massive, disseminated, brecciated and cemented by gangue minerals. Sphalerite is usually slightly transparent, sometimes with irregular alternating areas of optical zoning (Fig. 5a), either rich in internal reflections or darker and less transparent. Micro-inclusions of chalcopyrite, resembling chalcopyrite disease, are occasionally observed at the borders of sphalerite which also include relatively large amoeboidal tetrahedrite grains. Galena occurs as coarse-grained masses usually characterised by the presence of tetrahedrite blebs. Galena also commonly occurs as inclusions within other sulfides, mainly sphalerite and chalcopyrite. At Valbona, galena commonly also occurs as veinlets crosscutting coarse sphalerite grains. Chalcopyrite is commonly replaced by secondary covellite and goethite. Tetrahedrite is common as anhedral grains associated with the other sulfides, although it also occurs as stockwork veinlets (Camisolo lode) and as common blebby inclusions in galena (Fig. 5b). At Camisolo, tetrahedrite is sometimes fractured and cemented by a secondary mineral with dark greenish internal reflections (Fig. 5c). Pyrite occurs as coarse- to fine-grained euhedral crystals usually widespread in quartz gangue, but also associated with galena, sphalerite and chalcopyrite. At Camisolo and Valbona mines, pyrite can host tetrahedrite and galena blebs. Pyrite grains can also have Ni–Co sulfarsenide crystals in their cores. In general, pyrite seems to be the youngest of the most common sulfides. At Cortabbio, pyrite occurs as inclusions with chalcopyrite or as coarse-grained aggregates overgrown by Bi sulfosalts, and sometimes with an evident internal zoning underlined by colour variations. These observations suggest the presence of two different pyrite generations within the Cortabbio ore. Arsenopyrite is particularly abundant in the Valbona mine, whereas it is an accessory mineral in the Cortabbio veins. In the Valbona mine, arsenopyrite occurs as large, brecciated aggregates, associated locally with accessory bismuthinite, and interstitial to abundant subhedral pyrite grains affected by moderate fracturing (Fig. 5d). These brecciated aggregates are cemented by galena, sphalerite, tetrahedrite and gangue minerals of the main Valbona ore association. This arsenopyrite–pyrite ore facies seems to be older than the other sulfides of Valbona lode.

In the Cortabbio samples, two different ore assemblages were observed: sulfide rich and arsenide rich. In the sulfide-rich assemblage, the main observed sulfide is chalcopyrite, coupled with abundant disseminations of tetrahedrite, pyrite, galena and Ni–Co sulfarsenides. Diverse Ag–Bi sulfides and sulfosalts (up to 100 µm in size) occur as poly-granular blebs and lamellar aggregates commonly intergrown with the sub-millimetric galena inclusions (up to 500 µm; Fig. 6a) in chalcopyrite (Fig. 5e); the whitish grey-blue, Bi-bearing phases are easily distinguished from galena and from each other by their variable degree of pleochroism and anisotropy. Blebs of Bi-bearing sulfosalts, such as aikinite and various undetermined phases, were also observed. The quartz gangue is commonly disseminated with accessory small, white, euhedral, isotropic crystals (Fig. 5f), corresponding to zoned allocasite–glaucodot (Co,Fe)AsS (see section on Ni–Co–Fe arsenides and sulfarsenides below), in association with rutile.

In the Cortabbio arsenide-rich samples (Fig. 5g–j), the assemblage is dominated by Co-bearing Ni arsenides with a nodular to massive texture, in a gangue consisting of silicified host-rock fragments and hydrothermal carbonates (euhedral, bladed siderite and subordinate dolomite). The Ni–Co nodules grow over discontinuous carbonate selvages that pass laterally to micro-breccias with host schist fragments cemented by carbonates and accessory subhedral rutile. The cores of the arsenide nodules consist of rosettes of pink, pleochroic and strongly anisotropic nickeline (NiAs) with mosaic-like texture (Fig. 5h,i), radially overgrown by dense aggregates of white, pleochroic and anisotropic rammelsbergite lamellae (NiAs<sub>2</sub>) and, less commonly, by fine-grained, grey–white, isotropic aggregates of Ni–Co sulfarsenides. The nickeline rosettes start growing over carbonate or quartz micro-fragments as seeds. The external surface of the Ni–Co nodules is characterised by finely zoned crusts and minute, commonly euhedral, crystals of Ni–Co sulfarsenides (Fig. 6b). Ni–Co sulfarsenides overgrow both nickeline and rammelsbergite, but are also present as disseminated euhedral crystals, usually with a pyrite core, in the carbonate–quartz gangue. These disseminated crystals can be overgrown by galena and Bi sulfosalts. Extremely fine-grained native bismuth occurs in the interior of the arsenide nodules, as inclusions and along micro-fractures in nickeline and rammelsbergite, and as interstitial, coarse-grained aggregates easily mistaken for gold blebs (Figs 5j, 6b,c). The nodular Ni–Co arsenide mineralisation and related quartz–siderite gangue are affected by later baryte veining not easily discernible by optical microscopy, although evident in SEM–BSE imaging (Fig. 6d).

#### *NE–SW trending veins (base metal sulfide-dominated orebodies)*

In this base metal sulfide-dominated vein family, the most common sulfides are sphalerite, galena, chalcopyrite and pyrite. The ore minerals are semi-massive, disseminated, brecciated and cemented by gangue minerals, as observed for the NNW–SSE veins. Sphalerite is usually moderately transparent with red or brown internal reflections. Sphalerite commonly has chalcopyrite micro-inclusions, arranged according to regular patterns similar to chalcopyrite disease (Fig. 5k). In general, the sphalerite from NE–SW veins is characterised by a more extensive presence of chalcopyrite micro-inclusions compared to the sphalerite of the NNW–SSE veins. Galena has similar textures in both the NNW–SSE and NE–SW veins; however, it is characterised by the absence of Bi–Ag sulfosalts inclusions, with only sporadic tetrahedrite blebs at the Pra Piazza vein. At the Pra Piazza vein, tetrahedrite is also present as small anhedral masses associated with carbonate gangue. Chalcopyrite is commonly replaced by secondary covellite and goethite, as observed for the NNW–SSE veins. Chalcopyrite is generally not characterised by inclusions of other sulfides. Pyrite is present mainly as coarse- to fine-grained euhedral crystals in quartz gangue or associated with galena and sphalerite; sometimes with Ni–Co arsenide crystals as inclusions, in a similar fashion to that observed for the NNW–SSE veins. At Valle di Contra, pyrite can host galena inclusions.

Accessory minerals found in the samples from the Valle di Contra, Val Rossiga and Valtorta mines, are represented by hematite and magnetite inclusions in sphalerite (Fig. 5l) and rare Ni–Co sulfarsenide crystals, disseminated in quartz gangue. Sporadic small arsenopyrite crystals in quartz gangue can be observed at Valle di Contra. The gangue consists predominantly of quartz with minor Fe-carbonate and rare apatite in open space filling, although occasionally brecciated vein textures occur with silicified host-rock fragments affected by fine-grained disseminations of chalcopyrite and/or pyrite.



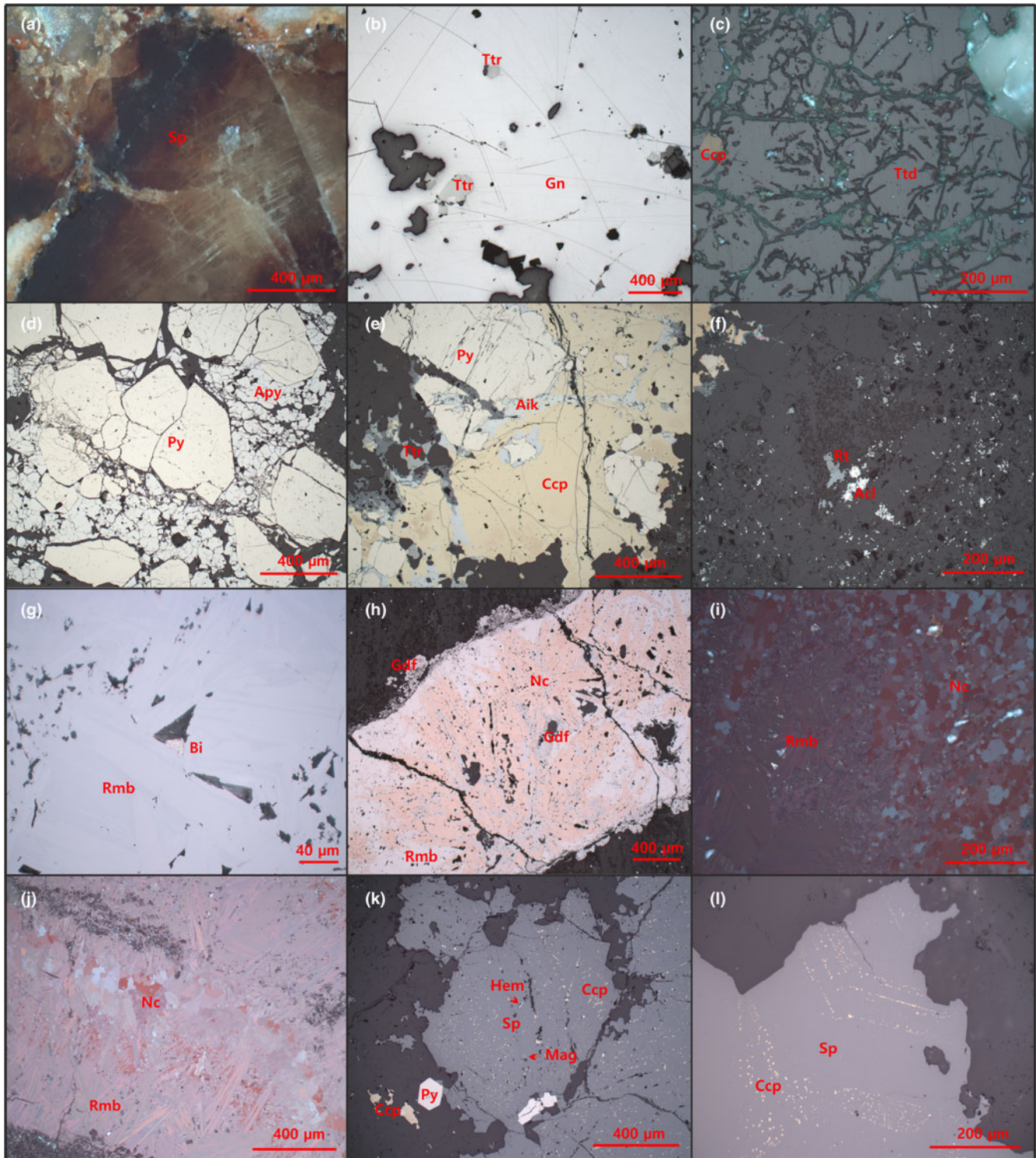


**Figure 5.** Microscopic features of ore minerals in the veins of the Valsassina mining district (reflected light microscopy). (a) A large sphalerite crystal displaying optical zoning with a homogeneously light coloured, transparent interior surrounded by a dark rim, Valbona mine. (b) Amoeboid inclusions of tetrahedrite (grey) in galena (white), Camisolo mine. (c) Cu-Sb-bearing alteration products with dark green internal reflections in tetrahedrite fractures. A yellow grain of chalcopyrite is also observable, Camisolo mine (crossed Nicols). (d) Euhedral yellowish white, subhedral pyrite crystals surrounded by interstitial arsenopyrite with marked brecciated texture, Valbona mine. (e) Light grey inclusions of galena and Ag-Bi-bearing sulfides and sulfosalts in chalcopyrite (associated with pyrite and tetrahedrite on the left), Cortabbio mines. (f) Small allosclerite and glaucodot white crystals in quartz gangue; some rutile grains (grey) are also observable (Cortabbio mines). (g) Massive Ni-Co-Fe arsenides in a veinlet from the Cortabbio mines. In the core of the aggregate, pink nickeline rosettes are overgrown (and partly replaced) by aggregates of greyish white, lamellar rammelsbergite crystals. Gersdorffite-cobaltite crusts (grey) grow on the external surface of the arsenide aggregate and also penetrate it, replacing both rammelsbergite and nickeline. (h) Native bismuth (yellowish) associated with rammelsbergite acicular crystals, Cortabbio mines. (i)(j) Crossed-Nicols microphotographs of nickeline rosettes, showing a peculiar mosaic texture, and, nearby, the aggregates of acicular crystals of rammelsbergite (Cortabbio mines). (k) Sphalerite rich in tiny chalcopyrite inclusions associated with minor hematite and magnetite (asterisks), Valtorta lode. (l) Sphalerite displaying chalcopyrite disease-like texture along thin bands in the Val Rossiga vein. All mineral name abbreviations are from Warr (2021).

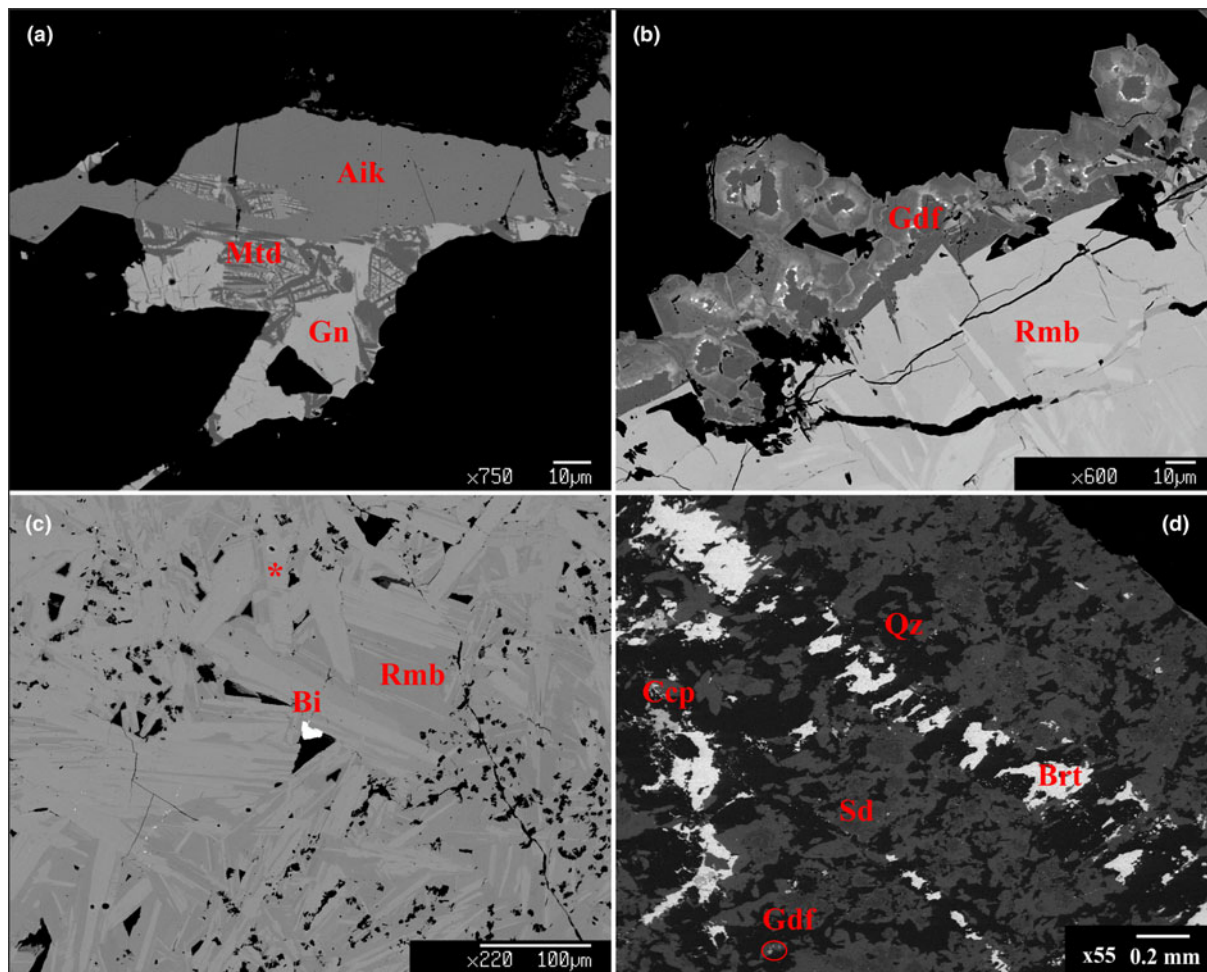


**Figure 6.** Microtextural (and microchemical) features of ore mineral species in the veins of the Valsassina mining district observed in SEM back-scattered electron imaging. (a) Exsolution lamellae of matildite (dark grey) in galena (light grey), associated with aikinite (mid-grey, upper part of the aggregate) from the Cortabbio mines. (b) Crust formed by zoned gersdorffite-cobaltite grains on the external surface of rammelsbergite aggregates (light grey lamellar crystals). Segregations of native bismuth (white inclusions) are visible in the gersdorffite-cobaltite growth zones (Cortabbio mines). (c) Zoned lamellar crystals of rammelsbergite associated with an interstitial grain of native bismuth; additional bismuth is also visible, as very small white inclusions, along a thin crack in rammelsbergite, in the lower left part of the image, Cortabbio Mines. (d) Baryte-chalcocopyrite veinlets evidently cut siderite and quartz in a Ni-Co-Fe nodule from Cortabbio mines. The siderite is zoned, with a Mg-rich core. Minor gersdorffite crystals are also present mainly in association with siderite.

A paragenetic scheme for the Valsassina veins is proposed in Fig. 7.

### Compositions of sulfides and sulfosalts

#### Sphalerite

Sphalerite from the base metal sulfide-dominating NE-SW vein system is represented by data from the Valle di Contra, Val Rossiga and Valtorta orebodies, whereas data from the Valbona, Cortabbio and Camisolo orebody are representative for sphalerite from the complex, ‘polymetallic’ mineralisation of the NNW-SSE vein system. The average trace-element concentrations of Valsassina sphalerite are shown in Table 2 (see also Supplementary Table S1 for the complete datasheet).

Iron and cadmium are the most abundant minor elements in sphalerite from all the investigated mineralised veins (Fig. 8a,b). In all the orebodies, sphalerite tends to be rather Fe-poor (Fig. 8a), with Fe contents higher than 2.50 wt.% only for the Valtorta, Camisolo veins and the base metal Valle di Contra veins, in which sphalerite has similar Fe contents ranging between

1.95 and 3.67 wt.% (average at 2.85, 2.97 and 2.93 wt.%, respectively; see Fig. 8a). The other veins (Cortabbio and Val Rossiga) have similar Fe concentrations (Fig. 8a), ranging between 0.19 and 1.00 wt.% (average at 0.63, 0.62 and 0.42 wt.%, respectively). Iron shows a clear inverse correlation with Zn (Fig. 8a,b).

In all the sampled veins, sphalerite displays a complex composition involving a wide range of accessory components. Cadmium is always present in all the analysed sphalerites, with contents varying from 1100 to over 5000 ppm. In particular, the Fe-poor sphalerites have slightly higher Cd contents (averages  $\approx$ 3300 ppm), with the exception of Valtorta sphalerite, that has Cd concentrations similar to the Fe-richer sphalerite (average  $\approx$ 2000 ppm). Cobalt has variable contents and higher concentrations in the Fe-enriched sphalerites (average 99.6 ppm compared to average 1.12 ppm of Fe-poor sphalerites), however the sphalerite from Valtorta has high Co concentrations coupled with low Fe contents (average 102.3 ppm, Fig. 8a). Compared to cobalt, nickel has very low concentrations (4.9 ppm maximum, often below detection). The Fe-enriched sphalerites from Valbona, Camisolo and Valle di Contra mines have higher concentrations of Mn,

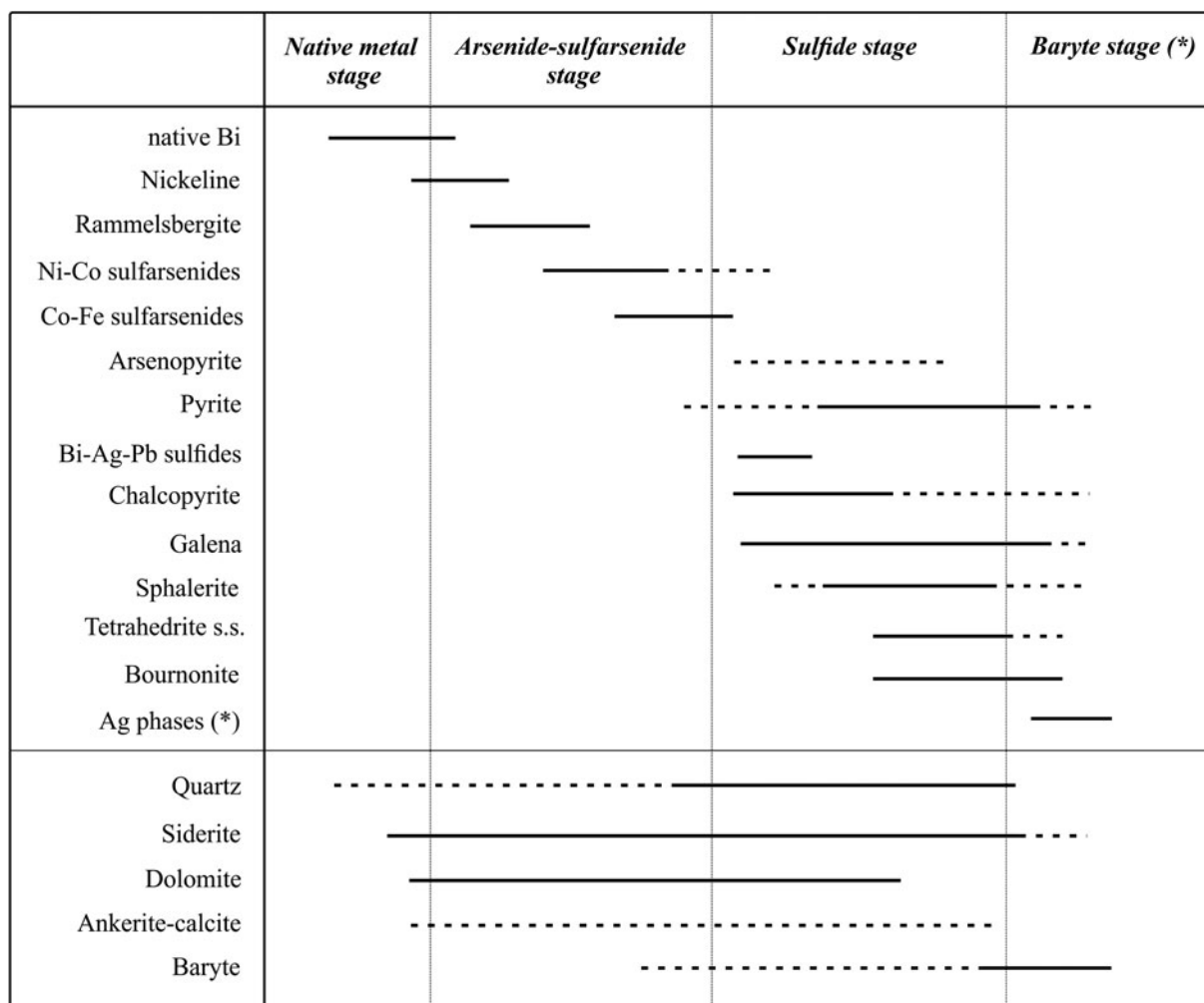


**Figure 7.** Preliminary paragenetic scheme of the Valsassina veins. In particular, the Ni-Co arsenide/sulfarsenide stage of Cortabbio has strong analogies with the so-called 'five-element veins'. Note that Ni-Co minerals are always older than the sulfides (\* potential baryte stage).

**Table 2.** Summary of sphalerite major and trace elements obtained by WDS and LA-ICP-MS analyses (see Supplementary Table S1 for the complete dataset).

Sample	NNW-SSE veins		NE-SW veins			
	Valbona VALB4	Cortabbio FD3	Camisolo CAM5	Valle di Contra CO1	Val Rossiga RO2	Valtorta VA3
Zn (wt.%)	63.7 (62.9–64.2)	65.8 (65.1–66.4)	63.7 (62.8–64.7)	64.0 (62.7–65.3)	66.0 (65.0–66.7)	65.9 (65.0–66.8)
Fe (wt.%)	2.9 (2.2–3.5)	0.6 (0.3–1.0)	3.0 (2.0–3.7)	2.9 (2.0–3.6)	0.6 (0.3–1.0)	0.4 (0.2–0.8)
Cd (ppm)	2931.6 (2108.7–6055.6)	3331.1 (3135.7–3596.9)	2175.9 (1449.1–3359.8)	2270.7 (1138.7–4249.8)	3135 (1895.1–5992.3)	2338.9 (1342.0–3229.3)
Co (ppm)	90.4 (37.3–123.8)	1.7 (0.7–5.5)	106.1 (50.6–220.4)	99.7 (71.3–124.2)	1.1 (0.3–2.0)	102.3 (56.2–138.4)
Ni (ppm)	0.1 (< d.l.–0.3)	0.9 (<d.l.–4.9)	0.1 (<d.l.–0.2)	0.03 (<d.l.–0.1)	0.05 (<d.l.–0.1)	0.7 (0.4–0.9)
Cu (ppm)	461.4 (61.9–989.9)	1864.6 (176.9–4734.1)	507.6 (45.8–1615.7)	255.7 (36.2–634.4)	1119.6 (55.9–4640.6)	3785.1 (69.2–7967.4)
Sb (ppm)	273.1 (19.2–947.0)	165.3 (16.9–447.6)	307.7 (4.1–1311.1)	111.8 (11.2–397.2)	147.5 (6.6–449.2)	873.0 (3.7–3551.0)
As (ppm)	5.9 (4.9–7.5)	16.0 (5.5–39.6)	6.2 (4.4–10.6)	5.5 (4.8–6.7)	13.3 (5.1–47.6)	32.5 (5.1–116.3)
Se (ppm)	<d.l.	<d.l.	<d.l.	<d.l.	<d.l.	<d.l.
Ga (ppm)	21.4 (1.0–46.6)	88.2 (8.0–339.6)	62.2 (4.8–265.6)	25.7 (0.6–121.1)	84.9 (3.2–198.3)	58.9 (0.7–110.6)
Ge (ppm)	69.4 (2.0–124.1)	16.4 (1.8–51.6)	37.5 (1.2–132.6)	39.3 (0.7–122.0)	15.0 (0.9–38.0)	2.6 (0.1–10.6)
In (ppm)	0.6 (0.01–5.6)	11.8 (0.1–20.8)	20.4 (0.01–140.7)	0.4 (0.1–0.6)	6.9 (0.08–17.9)	169.5 (6.0–831.5)
Mn (ppm)	10.3 (6.9–16.2)	2.7 (2.3–3.6)	11.4 (8.6–15.8)	10.4 (6.3–17.3)	2.6 (1.0–4.0)	9.2 (3.4–15.2)
Ag (ppm)	34.4 (7.4–114.6)	135.8 (27.5–524.0)	42.2 (6.0–161.3)	16.5 (5.4–48.7)	105.7 (20.9–325.8)	114.5 (4.1–490.9)
Sn (ppm)	8.7 (5.8–26.5)	9.0 (6.2–21.4)	17.6 (5.3–113.4)	5.6 (3.9–6.9)	10.7 (5.1–50.4)	18.2 (6.7–77.3)
Mo (ppm)	<d.l.	<d.l.	<d.l.	<d.l.	<d.l.	<d.l.

Data in wt.% or in ppm. The arithmetic mean (average), minimum and maximum values of 10 analyses are reported for every element.

The values under the detection limits '<d.l.' (reported in detail in Supplementary Table S1) were considered as 0 for the calculation of the average.

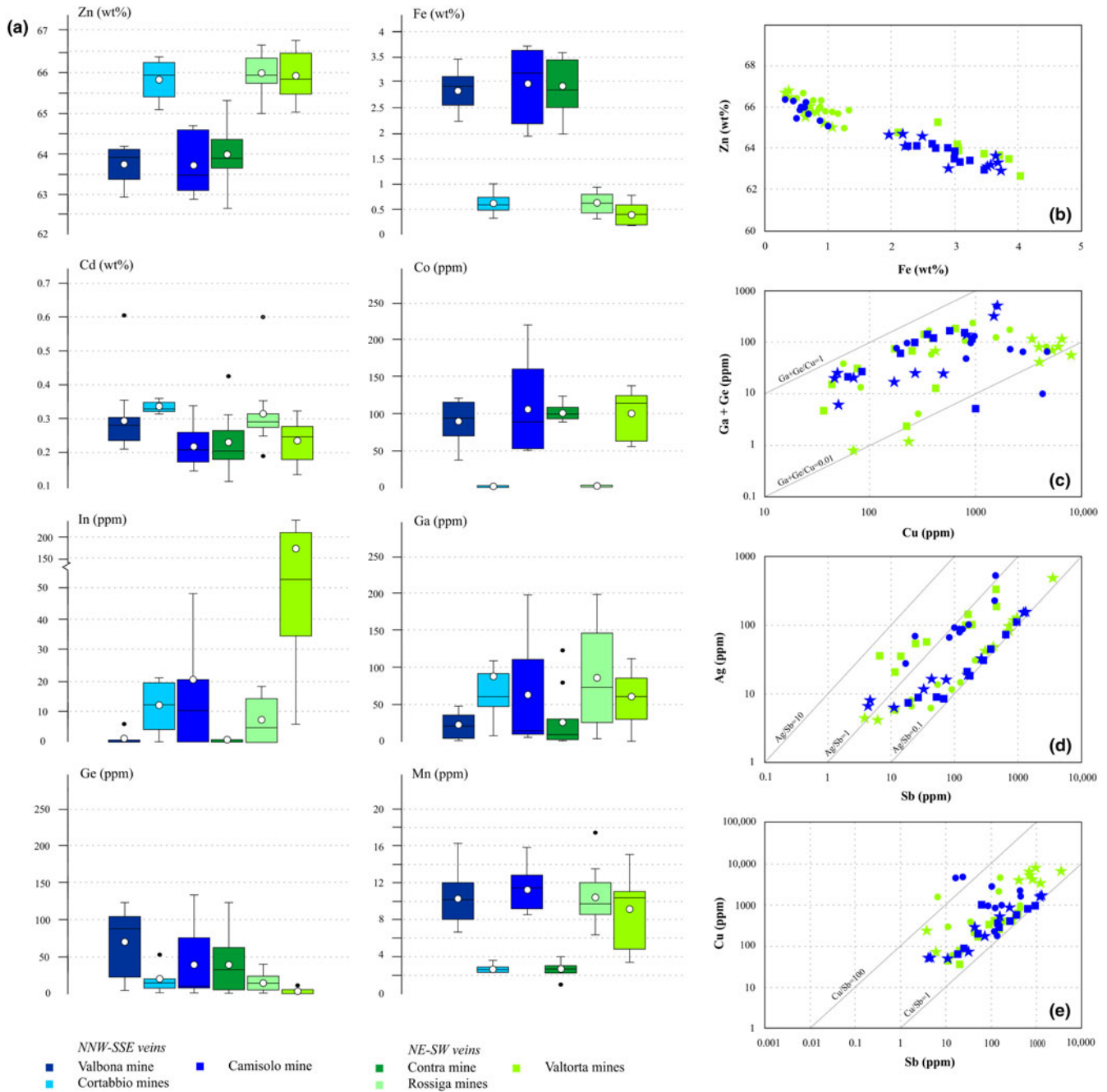


**Figure 8.** Major-, minor- and trace-element diagrams for sphalerite: (a) statistical dispersion box-plots of Zn, Fe, Cd, Co, In, Ga, Ge and Mn (for all the boxplots, the coloured box contains 50% of the data, the white dot indicates the mean, the horizontal continuous line the median and the black dots represent the outliers); (b) Zn vs. Fe; (c) Ga + Ge vs. Cu; (d) Ag vs. Sb and (e) Cu vs. Sb. Blue squares: Valbona; blue circles: Cortabbio; blue stars: Camisolo; green squares: Valle di Contra; green circles: Val Rossiga; green stars: Valtorta.

Cu and Ag, when compared to the Fe-poor sphalerites from Cortabbio, Val Rossiga and Valtorta veins (see Fig. 8a). Moreover, the sphalerite from the Valtorta vein has higher concentrations of In, Pb, As, Sb and Bi also with lower Ge concentrations (Fig. 8a), compared to the other veins (see Fig. 8a and Table 2). In general, Ga and Ge concentrations are correlated with Cu (Fig. 8c).

All the sphalerite samples are characterised by a direct correlation between Ag–Sb (Fig. 8d) and Cu–Sb (Fig. 8e). These correlations could suggest the presence of tetrahedrite micro-inclusions.

### Pyrite

The data set includes results from 60 LA–ICP–MS point analyses of pyrite crystals from the NNW–SSE and NE–SW veins and 10 analyses of crystals from the brecciated pyrite–arsenopyrite ore of the Valbona vein. The average major- and trace-element concentrations of the Valsassina pyrite are given in Table 3 (see also Supplementary Table S2 for the complete datasheet). Pyrite in internal cores of Ni–Co sulfarsenides were too small for LA–ICP–MS analyses.

Antimony, As, Cu, Pb, Ni and Zn are important trace elements within pyrite from the NNW–SSE and NE–SW veins and

compared to the Valbona brecciated pyrite, where Co is dominant (Fig. 9).

Pyrite in the NNW–SSE veins has higher Cu and Sb average contents, 1835 ppm and 2277 ppm respectively, compared to pyrite in the NE–SW veins (892 ppm and 1529 ppm, respectively). In contrast, the As values are similar for both the vein systems (1486 ppm for NNW–SSE veins pyrite and 1529 ppm for NE–SW veins pyrite). Copper, Sb and As are far less concentrated in the Valbona brecciated pyrite (Fig. 9), with averages of 0.42 ppm, 0.10 ppm and 18.95 ppm, respectively. However, the Val Rossiga pyrite is relatively lower in Cu, Zn, Pb, Ag and Sb when compared to the other pyrite from NE–SW veins and the NNW–SSE veins (Table 3). Averages of 33.6 ppm Zn and 146.2 ppm Pb for pyrite from the NNW–SSE veins, and 19.3 ppm Zn and 327.1 ppm Pb for the NE–SW veins, can be compared to the very low Zn and Pb contents (2.7 ppm Zn and 3.38 ppm Pb) for the Valbona brecciated pyrite. Regardless of the low concentrations, in the Valbona pyrite the concentration of Pb shows a direct correlation with Cu and Sb (Fig. 9a,b), suggesting the possible presence of rare bournonite micro-inclusions. Pyrites from the NNW–SSE and NE–SW veins also show a direct correlation between Sb–Cu (Fig. 9c) and Sb–Ag (Fig. 9d), suggesting the presence of a Cu–Zn–Ag–Sb-bearing phase (e.g. tetrahedrite) in these pyrites, in agreement with petrographic investigations.

Cobalt and Ni are minor components in pyrite for all the deposits (Fig. 9e). The Ni concentration ranges from 8 to 142 ppm (average 66 ppm) for the NNW–SSE veins and from 2 to 275 ppm for the NE–SW veins (average 65 ppm). The NNW–SSE and NE–SW pyrites are slightly Ni-enriched compared to the Valbona brecciated pyrite, which has Ni contents between 10 and 147 ppm (average 31 ppm). In contrast, Valbona brecciated pyrite is Co-enriched (11–223 ppm, average 79 ppm), compared to the NNW–SSE veins (15–8.90 ppm, average 2.50 ppm) and the NE–SW veins (0.003–81.58 ppm, average 5.30 ppm). Therefore, the Valbona brecciated pyrite has higher Co/Ni ratios (between 0.69 and 5.34, average 3.21) compared to the NNW–SSE veins (0.003–0.21, average 0.05) and the NE–SW veins (0.001–0.61, average 0.08).

All pyrites are depleted in Se, generally under the detection limit or with concentrations that do not exceed 35 ppm. The pyrites are also Te, Au, Tl, Mo and V poor, however the pyrites from the NNW–SSE and NE–SW veins are, in general, relatively more enriched in these elements compared to the Valbona brecciated pyrite.

#### Tetrahedrite

The major-element compositional data of the tetrahedrite solid solution (*s.s.*) (Supplementary Table S3a) show remarkable differences between the tetrahedrites in the Valbona, Cortabbio and Camisolo veins. The Valbona tetrahedrite displays minimal As content (<0.95 wt.%), representing a near end-member tetrahedrite, and with Ag content from 2.91 to 2.97 wt.%. In the tetrahedrite of the Camisolo lode, the Sb/As ratios vary from 4:1 to 7:1, indicating the occurrence of tetrahedrite with minor As (up to 4.97 wt.%), and with Ag contents varying between 1.14 and 1.45 wt.%. The tetrahedrite *s.s.* of the Cortabbio lode has Sb/As ratios of 1:4, therefore tends towards the As end-member tennantite (As 16.08–16.70 wt.%, Sb 4.44–5.41 wt.%), with a narrow range of Ag concentration (between 3.12 and 3.42 wt.%). In addition, significant differences are observed for Fe and Zn (Supplementary Table S3a). In the Camisolo and Valbona As-poor tetrahedrite, Zn is dominant over Fe, whereas the tennantite from Cortabbio is Fe-rich. The general compositional

formulae of tetrahedrite/tennantite, calculated on the basis of 13 S atoms per formula unit, are:  $(\text{Cu}_{9.20-9.47}\text{Fe}_{0.29-0.39}\text{Zn}_{1.53-1.61}\text{Ag}_{0.17-0.21})\Sigma_{11.19-11.68}(\text{As}_{0.43-1.11}\text{Sb}_{2.56-3.71})\Sigma_{3.67-4.14}\text{S}_{13}$  for the Camisolo lode,  $(\text{Cu}_{9.12-9.17}\text{Fe}_{0.83-0.89}\text{Zn}_{1.18-1.19}\text{Ag}_{0.46-0.47})\Sigma_{11.59-11.72}(\text{As}_{0.14-0.21}\text{Sb}_{3.98-4.01})\Sigma_{3.67-4.14}\text{S}_{13}$  for the Valbona lode and  $(\text{Cu}_{9.07-9.12}\text{Fe}_{1.13-1.17}\text{Zn}_{0.82-0.89}\text{Ag}_{0.43-0.47})\Sigma_{11.45-11.65}(\text{As}_{3.24-3.34}\text{Sb}_{0.54-0.67})\Sigma_{3.88-3.91}\text{S}_{13}$  for the Cortabbio mine. The EMPA–WDS analyses also indicated that the Valsassina tetrahedrites are rather poor in accessory elements, generally close to or below instrumental detection limits with the exception of Pb, probably due to contamination by host galena and localised Ni enrichments (at Camisolo).

#### Ni–Co–Fe arsenides and sulfarsenides

Ni–Co–Fe sulfarsenides and Ni arsenides are well represented in the Cortabbio lodes; whereas, in the base metal-rich veins, Ni–Co sulfosalts are subordinate and represented by rare sulfarsenide with gersdorffite composition, usually occurring as micro-inclusions in the cores of euhedral pyrite crystals disseminated in quartz gangue. Supplementary Table S3b shows the EMPA–WDS data for the Ni–Co phases observed in this investigation.

The Ni arsenides, which characterise only the Ni–Co-rich facies of the Cortabbio lode, are represented by nickeline (NiAs) and rammelsbergite (NiAs<sub>2</sub>). Nickeline is basically pure, whereas rammelsbergite, associated with gersdorffite in the external portions of the nodules, has some compositional variation, due to incorporation of Co replacing Ni (max 5.47 wt.% Co). Rammelsbergite has a general compositional formula of  $\text{Ni}_{0.84-1.00}\text{Co}_{0-0.19}\text{As}_2$ , whereas nickeline is stoichiometrically pure.

Ni–Co–Fe sulfarsenides occur most commonly and are represented by phases with variable compositions, here listed in order of abundance: gersdorffite with or without Sb and Co (ullmannite and cobaltite components, respectively); alloclasite–cobaltite; and glaucodot. The external sulfarsenide crusts of the Cortabbio Ni–Co–Fe nodules are composed mainly of gersdorffite. Gersdorffite has variable compositions, with substitutions of Sb for As and of Co for Ni. In general, gersdorffite at Cortabbio is characterised by a variable ullmannite component due to irregular incorporation of Sb (up to 9.84 wt.%). The general compositional formula of the Cortabbio gersdorffite, calculated on the basis of one S atom per formula unit, is:  $(\text{Ni}_{0.63-0.97}\text{Co}_{0-0.23})\Sigma_{0.86-0.97}(\text{As}_{0.81-1.03}\text{Sb}_{0-0.13})\Sigma_{0.94-1.03}\text{S}$ . However, the sulfarsenide crusts also have a less common phase with a Ni-rich cobaltite composition (with 19.01 wt.% Co and 10.89 wt.% Ni). Alloclasite and glaucodot are commonly present as small euhedral crystals disseminated in quartz gangue in the sulfide-rich ore association of Cortabbio. Alloclasite has Co and Fe contents ranging between 19.73 and 24.34 wt.% and between 8.2 to 9.87 wt.%, respectively (Supplementary Table S3b). In glaucodot, Co and Fe range between 9.58–15.64 wt.% and 17.18–25.17 wt.%, respectively. Both of these minerals also contain minor components such as Ni and Cu, with up to 2.26 wt.% Ni and up to 6.08 wt.% Cu, the latter probably related to (sub-)micro-inclusions of chalcopyrite or tetrahedrite. The general compositional formulae of the two minerals, calculated on the basis of one S atom per formula unit, are:  $(\text{Co}_{0.68-0.70}\text{Fe}_{0.29-0.30}\text{Ni}_{0-0.07})\Sigma_{0.97-1.07}\text{As}_{1.06-1.07}\text{S}$  for alloclasite and  $(\text{Fe}_{0.55-0.74}\text{Co}_{0.29-0.41})\text{As}_{1.04-1.09}\text{S}$  for glaucodot.

#### Other sulfides and sulfosalts

Arsenopyrite is a major mineral only in the distinct brecciated arsenopyrite–pyrite ore facies in the Valbona lode, and shows minimal compositional variability and As contents compatible

**Table 3.** Summary of pyrite trace-element data obtained by LA-ICP-MS analyses (see Supplementary Table S2 for the complete dataset).

sample	NNW-SSE veins				NE-SW veins		
	Valbona (cataclastic) VALB3	Valbona VALB4	Cortabbio FD3	Camisolo CAM5	Valle di Contra CO1	Val Rossiga RO2	Valtorta VA3
Fe (wt.%)	46.2 (45.9–46.3)	46.2 (46.0–46.2)	46.1 (46.0–46.3)	46.3 (45.9–46.9)	46.4 (46.3–46.9)	46.2 (45.7–46.4)	46.2 (46.1–46.2)
S (wt.%)	53.1 (50.9–53.6)	50.9 (50.1–52.8)	50.1 (47.3–52.8)	51.2 (49.4–53.2)	51.3 (49.8–52.9)	52.7 (50.7–52.9)	50.8 (49.7–52.3)
Co (ppm)	78.6 (11.2–222.6)	2.0 (0.4–23.8)	2.9 (0.1–8.9)	2.5 (0.6–5.8)	2.2 (0.4–4.5)	10.7 (0.003–81.6)	2.9 (0.5–6.0)
Ni (ppm)	31.8 (10.1–147.6)	61.1 (30.0–88.1)	78.9 (18.0–123.6)	59.6 (8.4–105.6)	81.7 (6.9–81.7)	27.1 (2.5–132.8)	86.8 (39.5–274.8)
Cu (ppm)	0.4 (0.1–1.0)	2264.9 (760.2–4995.1)	2194.9 (346.8–5872.7)	1044.3 (17.8–2980.0)	941.5 (89.2–2376.5)	90.8 (23.5–174.1)	1644.1 (351.4–3664.4)
Zn (ppm)	2.7 (0.7–9.4)	48.9 (11.8–300.2)	18.17 (5.9–24.2)	33.7 (6.8–118.7)	19.1 (4.7–27.9)	4.6 (2.8–8.7)	34.4 (6.2–117.7)
Pb (ppm)	3.38 (0.008–12.9)	165.9 (17.3–482.6)	79.3 (4.2–186.4)	193.3 (22.6–669.2)	248.2 (2.8–541.6)	53.8 (15.1–194.1)	679.2 (60.7–3310.5)
Sb (ppm)	0.1 (< d.l.–0.3)	2300.8 (1827.9–3101.3)	2812.4 (339.3–5373.0)	1717.9 (180.8–3234.0)	1730.6 (468.6–3064.2)	133.0 (64.4–279.6)	2066.2 (512.6–3068.5)
As (ppm)	19.0 (10.2–32.7)	1463.1 (1053.1–2725.5)	1441.1 (911.3–2482.9)	1554.0 (906.4–2537.0)	1508.9 (1027.5–2222.2)	1605.4 (404.3–6491.6)	1473 (1055.7–2428.7)
Se (ppm)	<d.l.	<d.l.	<d.l.	<d.l.	<d.l.	<d.l.	<d.l.
Tl (ppm)	<0.1 (<d.l.–0.035)	0.7 (0.2–3.1)	1.2 (0.2–6.1)	0.6 (0.01–3.2)	0.4 (0.02–2.0)	5.3 (2.5–11.8)	0.4 (0.1–1.3)
Ga (ppm)	<0.01 (<d.l.–0.019)	0.3 (0.04–1.0)	0.2 (0.1–0.5)	0.2 (<d.l.–0.5)	0.2 (<d.l.–0.6)	0.1 (<d.l.–0.7)	0.3 (0.009–0.7)
Ge (ppm)	0.1 (<d.l.–0.3)	0.04 (<d.l.–0.1)	0.1 (<d.l.–0.2)	0.05 (<d.l.–0.1)	0.1 (0.03–0.5)	0.1 (0.03–0.1)	0.1 (<d.l.–0.1)
Bi (ppm)	1.9 (0.02–4.3)	2.3 (0.2–14.3)	2.1 (0.04–6.5)	1.8 (0.6–7.9)	3.9 (0.1–11.3)	2.0 (0.03–6.7)	5.3 (0.1–19.8)
Mo (ppm)	<d.l.	<d.l.	<d.l.	<d.l.	<d.l.	<d.l.	<d.l.
Ag (ppm)	0.1 (<d.l.–0.046)	76.7 (58.2–105.1)	119.4 (11.8–231.2)	52.3 (2.6–100.8)	54.9 (7.9–100.8)	7.9 (2.5–22.0)	70.2 (14.3–100.9)
Hg (ppm)	11.0 (7.7–17.5)	19.4 (12.1–30.4)	14.3 (11.1–17.6)	18.2 (9.6–39.1)	26.0 (14.6–39.3)	21.8 (15.3–26.7)	19.9 (4.4–33.1)
V (ppm)	0.01 (0.006–0.020)	1.8 (0.3–3.5)	1.8 (0.3–1.8)	1.0 (0.02–3.2)	1.3 (0.2–3.8)	1.1 (0.01–7.5)	1.0 (0.07–1.9)
Ti (ppm)	0.1 (<d.l.–0.4)	0.7 (0.04–1.5)	3.0 (<d.l.–18.3)	1.4 (0.1–4.0)	3.2 (<d.l.–14.9)	29.4 (0.4–242.2)	0.8 (<d.l.–2.4)
Rb (ppm)	0.1 (<d.l.–0.4)	0.9 (0.1–2.5)	1.1 (0.2–3.9)	0.9 (0.02–2.1)	1.6 (0.03–5.0)	0.8 (<d.l.–5.7)	1.2 (<d.l.–3.9)
Sr (ppm)	0.2 (<d.l.–1.3)	0.5 (0.2–0.7)	0.5 (0.2–1.3)	0.3 (0.01–0.5)	0.3 (0.03–0.7)	0.2 (0.01–1.0)	0.6 (0.1–1.3)
Zr (ppm)	<d.l.	<d.l.	<d.l.	<d.l.	<d.l.	<d.l.	<d.l.
Cs (ppm)	0.3 (<d.l.–1.1)	1.6 (0.7–2.6)	1.5 (0.4–2.5)	1.3 (0.1–3.4)	1.3 (0.1–2.4)	0.1 (<d.l.–0.6)	1.4 (0.1–2.1)
Ba (ppm)	0.5 (<d.l.–3.1)	1.9 (0.6–2.7)	2.7 (1.2–5.9)	1.4 (<d.l.–2.8)	2.3 (0.1–5.2)	2.6 (0.6–8.7)	3.8 (0.1–14.7)

Data in wt.% or in ppm. The arithmetic mean (average), minimum and maximum values of 10 analyses are reported for every element. The values under the detection limits (reported in detail in Supplementary Table S2) were considered as 0 for the calculation of the average.

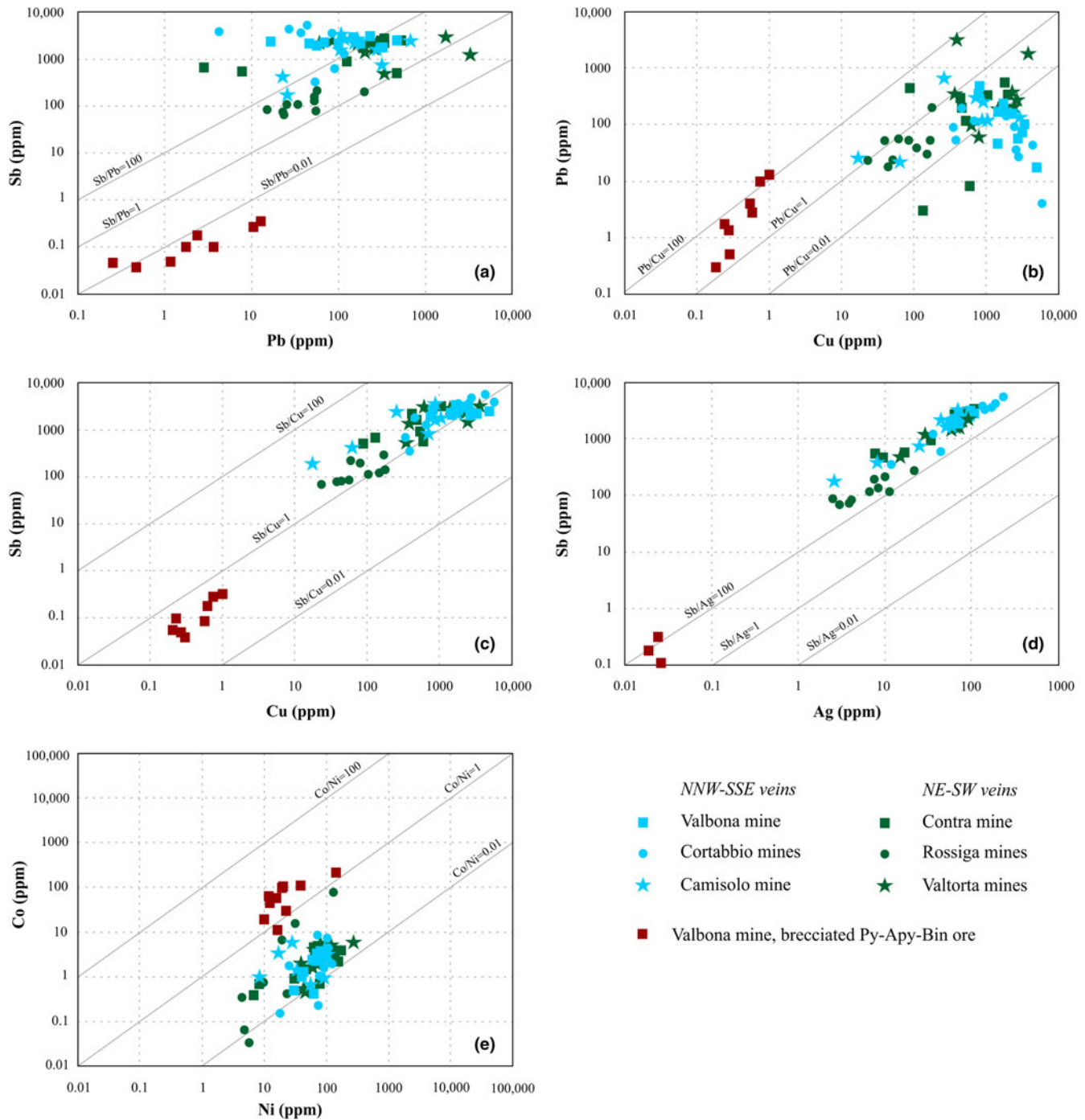


Figure 9. Trace-element binary plots of the pyrite compositional data: (a) Sb vs. Pb; (b) Pb vs. Cu; (c) Sb vs. Cu; (d) Sb vs. Ag; (e) Co vs. Ni.

with its association with pyrite (Supplementary Table S3b). In the Valbona mine, bismuthinite is present as micrometric inclusions in pyrite associated with arsenopyrite. Bismuthinite has accessory contents of Pb (0.6 wt.%), Sb (0.14 wt.%) and Ag (0.04 wt.%) (Supplementary Table S3c). As noted above, in the chalcopyrite-galena ore facies of the Cortabbio lode, diverse Ag-Bi sulfides and sulfosalts were observed (Supplementary Table S3c). The most common, aikinite, already reported by Guastoni *et al.* (2015) for the Cortabbio lode, is nearly stoichiometric, with formula  $Pb_{0.95}Cu_{0.92}Bi_{1.01}S_3$ . Matildite is the second most common Bi-bearing metallic mineral at Cortabbio and has a calculated

formula of  $Ag_{0.99}Bi_{0.98}S_2$ . Minor wittichenite (calculated formula  $Cu_{3.05}Bi_{0.97}S_3$ ) and rare ourayite are associated with matildite. Only one, out of the rare micro-blebs of presumed ourayite, was suitable for EMPA-WDS analysis. The calculated formula for this sulfosalts is  $Ag_{2.70}Cu_{0.27}Pb_{3.87}Bi_{4.95}S_{13}$ , in good agreement with the ideal composition.

#### Carbon and oxygen isotope data in ore-related carbonates

The isotopic  $\delta^{13}C$  and  $\delta^{18}O$  composition of the gangue carbonates (siderite and dolomite), from polymetallic and base metal

sulfide-rich vein systems, is reported in Supplementary Table S4. Data are plotted in Fig. 10. Polymetallic veins are represented by siderite-rich samples only (representing both Ni–Co–arsenide ore and sulfide–tetrahedrite assemblages), whereas base metal sulfide-rich veins are represented by samples where either siderite or dolomite are the dominant carbonate species. In the  $\delta^{18}\text{O}$  (V-SMOW) versus  $\delta^{13}\text{C}$  (V-PDB) diagram (Fig. 10a), most of the Valsassina data plot in an elliptic cloud characterised by moderately negative  $\delta^{13}\text{C}$  values (with low variability: between  $-1$  and  $-5$  *per mil*), and by  $\delta^{18}\text{O}$  spread over a slightly wider range (between  $+14$  and  $+20$  *per mil*). Only one sample plots at lower  $\delta^{13}\text{C}$  values, at  $-8.5$  *per mil*. Dolomite-dominated samples tend to plot at relatively heavier  $\delta^{13}\text{C}$  values, although their difference with siderite, both in terms of  $\delta^{13}\text{C}$  and  $\delta^{18}\text{O}$  signatures, is minor. Supplementary Table S4 also reports evaluation of the isotopic composition of the mineralising fluids in equilibrium with the ore-related siderite and dolomite gangues (Fig. 11), by employing mineral–fluid fractionation equations as a function of temperature for siderite and dolomite *vs.* water and  $\text{CO}_2$ , respectively by Zheng (1999; equations 1 and 2) and by Golyshev *et al.* (1981; equations 3 and 4):

$$1000 \ln \alpha_{\text{siderite-water}} = 4.23 \cdot 10^6 / T^2 + (-4.58 \cdot 10^3 / T) + 1.73 \quad (1)$$

$$1000 \ln \alpha_{\text{dolomite-water}} = 4.06 \cdot 10^6 / T^2 + (-4.65 \cdot 10^3 / T) + 1.71 \quad (2)$$

$$1000 \ln \alpha_{\text{siderite-CO}_2} = 0.07707 \cdot 10^{18} / T^6 + (-5.8544 \cdot 10^{12} / T^4) + 31.81548 \cdot 10^9 / T^3 + (-63.55559 \cdot 10^6 / T^2) + 51.46659 \cdot 10^3 / T - 12.36038 \quad (3)$$

$$1000 \ln \alpha_{\text{dolomite-CO}_2} = 0.07579 \cdot 10^{18} / T^6 + (-5.76702 \cdot 10^{12} / T^4) + 31.37431 \cdot 10^9 / T^3 + (-62.58142 \cdot 10^6 / T^2) + 49.20807 \cdot 10^3 / T - 11.39305 \quad (4)$$

where  $\alpha$  represents the isotope fractionation and  $T$  is the temperature in  $^\circ\text{C}$ . The calculation was performed using the *Web Stable Isotope Fractionation Calculator* by Beaudoin and Therrien (2009).

## Discussion

Petrography, compositional features of sphalerite, pyrite and associated minerals, together with stable isotope analyses of carbonates, were employed in order to highlight the differences or analogies between the sulfide assemblages of the NNW–SSE (polymetallic) *vs.* the NE–SW (base metal sulfide-rich) vein families, as well as to compare these ore deposits with similar ore systems.

### Ore petrography and composition of major and accessory phases

The petrographic features of the sulfide-rich assemblages of the two vein families are broadly similar, although the NE veins

display a simpler, basic assemblage due to the dominant presence of sphalerite, whereas chalcopyrite, galena and pyrite are only rarely accompanied by accessory sulfides and sulfosalts (e.g. tetrahedrite and Ag–Bi-bearing phases). Pyrite, in particular, has identical features in both the vein families. It is also important to consider that the pyrite grains from both the NE–SW and the NNW–SSE veins commonly contain Ni–Co sulfarsenides in their cores. In both vein families, sphalerite is characterised by the development of a chalcopyrite disease-like texture, following more or less regular patterns. However, in some of the base metal sulfide-rich veins, this texture in sphalerite is more intensely developed and micro-inclusions of magnetite and hematite occur together with the overwhelming inclusions of chalcopyrite. As previously reported, pyrite and sphalerite from both vein systems are probably characterised by the presence of micro-inclusions of possible Ag-bearing tetrahedrite, as suggested by the LA–ICP–MS analyses. However, Ni–Co sulfarsenides, arsenopyrite, tetrahedrite and bournonite are also present as accessory minerals in the NE–SW vein family. Considering this, it seems that the NE–SW and NNW–SSE veins are not defined by distinct parageneses, but rather by varying relative abundances of the metallic minerals.

Sphalerite can host a wide range of minor and trace elements, according to compositional patterns that are considered as sensitive to variations of depositional conditions (widely reviewed in Cook *et al.*, 2009a). In our study, the sphalerite data for Cd, Mn, Ga, Ge, Ni, Se, Bi, As, Sn and Ag do not help in discriminating between the polymetallic vein family and the base sulfide-rich family, whereas Fe, Co and In display markedly different signatures for the various orebodies, although independently from assemblages and structural orientation, as shown in Fig. 8a. The higher Fe contents sharply distinguish the Valbona, Camisolo and Valle di Contra lodes from all the others (Fig. 8a,b). Cobalt also contributes to this discrimination: it occurs in sphalerite from all veins, but it is less markedly enriched in the Fe-poor sphalerite of the Cortabbio and Val Rossiga lodes. A possible explanation of such cobalt distribution may be compatible with the presence or absence of other phases (e.g. arsenides) that preferentially incorporate Co, and sequester it from the fluid where sphalerite may subsequently crystallise. Indium displays low contents, typically below 1 ppm, and an irregular distribution in both vein systems, although it tends to be particularly enriched (median over 50 ppm and up to 830 ppm) in the Valtorta mine (Fig. 8a). Antimony and Cu are more enriched in the Valtorta sphalerite, however this is probably due to the presence of tetrahedrite-like inclusions; indeed, Sb *vs.* Cu and Sb *vs.* Ag show a clear direct correlation in Valsassina sphalerite.

Previous studies have shown that the divalent cations Mn, Cd, Co, Cd and Fe can directly replace Zn in the sphalerite structure (e.g. Cook *et al.*, 2009a; Ye *et al.*, 2011). However, Cook *et al.* (2012) and Belissont *et al.* (2014) also demonstrate incorporation of trivalent and tetravalent cations, such as  $\text{Ga}^{3+}$ ,  $\text{In}^{3+}$  and probably  $\text{Sn}^{3+}$  or  $\text{Sn}^{4+}$ , coupled with the monovalent Cu and Ag. Gallium and Ge are always detected in sphalerites from all veins with maximum contents of  $\sim 340$  ppm and 130 ppm, respectively. A positive correlation was observed between Cu and Ga in all the sphalerite samples, supporting the coupled substitution  $2\text{Zn}^{2+} \leftrightarrow \text{Cu}^+ + \text{Ga}^{3+}$ . There is also a positive correlation between Cu and Ge (as well as between Cu and Ga+Ge) in all the analysed sphalerite spots (Fig. 8d), suggesting the presence of the coupled substitution  $2\text{Cu}^+ + \text{Ge}^{4+} \leftrightarrow 3\text{Zn}^{2+}$  which could point to reducing conditions in the ore-forming fluids (Cook *et al.*, 2009a; Ye *et al.*, 2011; Belissont *et al.*, 2014). However, in these veins the



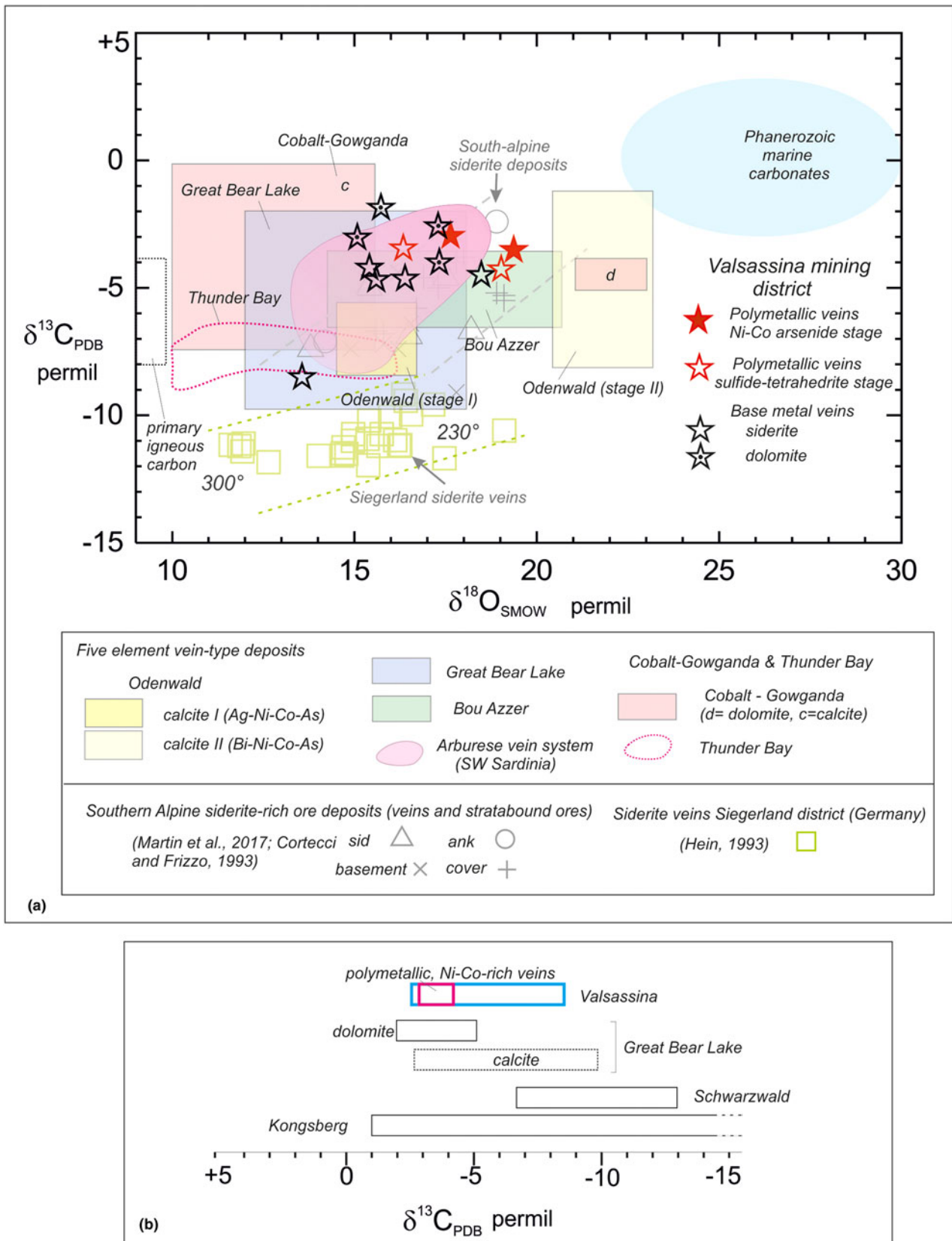


**Figure 10.** Carbon and oxygen isotope composition of ore-related carbonates in the Valsassina veins: the  $\delta^{18}\text{O}$  (V-SMOW) and  $\delta^{13}\text{C}$  (V-PDB) diagram in (a) and the  $\delta^{13}\text{C}$  (V-PDB)-only plot in (b) display the isotopic signatures of siderite and dolomite from the base metal sulfide-rich and polymetallic veins, and compare them with several datasets from worldwide five-element vein-type deposits.

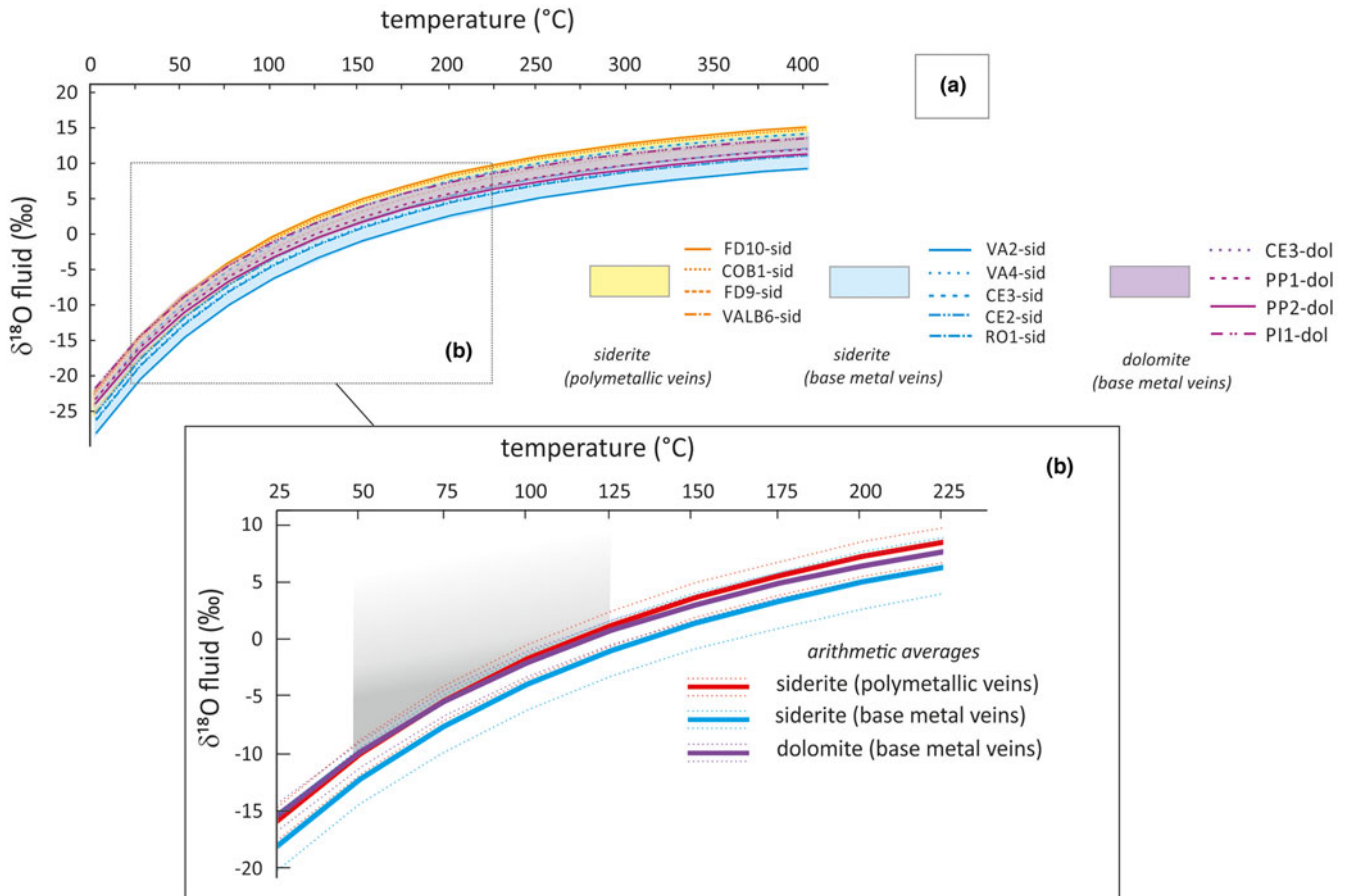


**Figure 11.** (a) Mineral–fluid fractionation curves based on  $\delta^{18}\text{O}$ ‰ V-SMOW of siderite and dolomite in samples from polymetallic veins and from base metal veins within the Valsassima hydrothermal system. (b) Detail of (a) with the plot of the arithmetic averages of each group of mineral–water fractionation curves.

absence of pyrrhotite, and the occurrence of baryte as common gangue mineral and of magnetite + hematite inclusions in sphalerite from the Valtorta and Rossiga samples, are not compatible with markedly reducing conditions.

In addition to sphalerite, pyrite in the Valsassima veins was analysed in detail as it has been found that the trace-element composition of pyrite, when considering elements such as Co, Ni, As, Sb, Se, Zn, Cu, Pb and Ag can contribute to the characterisation of the genesis of hydrothermal ore deposits (Cook and Chryssoulis, 1990; Cook *et al.*, 2009b; Deditius *et al.*, 2009; Deditius *et al.*, 2014; Genna and Gaboury, 2015; Large *et al.*, 2009; Reich *et al.*, 2005; Reich *et al.*, 2013). Trace elements in pyrite can be usually divided into three different groups (e.g. Wang *et al.*, 2018 and reference therein): (1) a group including elements that can enter the iron sulfide crystal structure due to substitution of iron, such as Co, Ni and Tl, or due to substitution of sulfur, such as As, Se and Sb (these elements can be also hosted by micro- or nano-inclusions); (2) a group consisting of elements, such as Cu, Zn, Pb and Ag, usually hosted by inclusions of other sulfide minerals; (3) a group characterised by high field strength and lithophile elements (such as Zr, La, Th, U and Ba), which most probably are hosted as oxides or silicate inclusions in the iron sulfides.

Cobalt and Ni often display a similar geochemistry to Fe and do not change their concentrations during pyrite recrystallisation and can be easily incorporated into its crystal structure (e.g. Large *et al.*, 2009; Koglin *et al.*, 2010). Because of this, the Co/Ni ratio of

pyrite has been considered useful in discriminating pyrite of different origins (e.g. Price, 1972; Bralía *et al.*, 1979). High Co and Ni concentrations and high Co/Ni ratios (Co/Ni > 1) in pyrite might suggest an origin ascribable to a hydrothermal regime (Bralía *et al.*, 1979). In contrast, pyrite associated with a sedimentary environment usually has low Co/Ni ratios (<1, Ni-dominated). Hydrothermal pyrite can also have Co/Ni ratios < 1, in which case it is necessary to consider, for example, geological and mineralogical features, together with the genetic type of ore deposit (Bralía *et al.* 1979), for an unambiguous distinction.

The pyrites from the NNW–SSE and NE–SW veins have low Co and Ni contents (average Ni 66 ppm and Co 3.99 ppm) with a Co/Ni ratio ranging from 0.001 to 0.61 (mean 0.05 and 0.08, for NNW–SSE and NE–SW veins, respectively). Similarly, the Valbona brecciated pyrite has low Co and Ni contents (average Ni 31.8 ppm and Co 78.6 ppm), however it has Co/Ni ratios ranging from 0.69 and 5.34 (average 3.21), very different from those observed for the other pyrite. In general, all the pyrite studied have Ni–Co contents and Co/Ni ratios far lower than what was expected for porphyry Cu deposits and other magmatic-related ore deposits, suggesting the lack of dominant hydrothermal fluids firmly ascribable to magmatic activity.

According to recent studies (Rajabpour *et al.*, 2017; Li *et al.*, 2021), the As concentration in pyrite may reflect the proportion of meteoric to magmatic waters within the system, with meteoric or basinal water abundances correlating positively with pyrite As concentrations. In contrast, mineralising fluids with higher

abundance of magmatic waters would tend to form pyrite with higher concentrations of Co and lower concentrations of As. The pyrites from Valsassina veins are characterised by high As concentrations, on average  $\approx 1500$  ppm, whereas the Valbona brecciated pyrites have low As concentration (average 18 ppm). The pyrites from the NNW–SSE and NE–SW veins plot close to the As apex in a Co–Ni–As diagram (Fig. 12), indicating that this pyrite may have been formed from hydrothermal fluids with a major component derived from surficial, meteoric waters. Instead, the data for the Valbona brecciated pyrite are dispersed towards the Co apex across the magmatic–hydrothermal/epithermal field, thereby suggesting an origin from a different context, or a different fluid, possibly with a deep component (Fig. 12).

### Estimation of the temperatures of ore formation

Variations in sphalerite composition can be used for thermo- and barometric evaluation (e.g. Kullerud, 1953), for geothermometry (Frenzel *et al.*, 2016), for discriminating between different genetic settings (e.g. Qian, 1987; Schwartz, 2000) and for tracking changes in ore/fluid interaction in a given ore deposit (e.g. Gottesmann and Kampe, 2007; Gottesmann *et al.*, 2009). In the absence of fluid-inclusion analyses, preliminary temperature estimates for the Valsassina vein systems can be based on the sphalerite composition. As noted above, analyses of the accessory elements of sphalerite can be used to evaluate the temperature of the orebodies. In particular, here we apply the GGIMFis geothermometer of Frenzel *et al.* (2016) which is based on Ga, Ge, In, Mn and Fe contents of sphalerite. The estimated temperatures for the Valsassina orebodies, in Supplementary Table S4 for all the veins, lies in the range 135–192°C. The estimated temperatures for the Camisolo, Valbona, Rossiga, and Valtorta veins (160–190°C) are slightly higher than those obtained for the Cortabbio and Contra veins (130–140°C). These data highlight another similarity between the two vein systems. They share quite similar temperature ranges, which are generally indicative

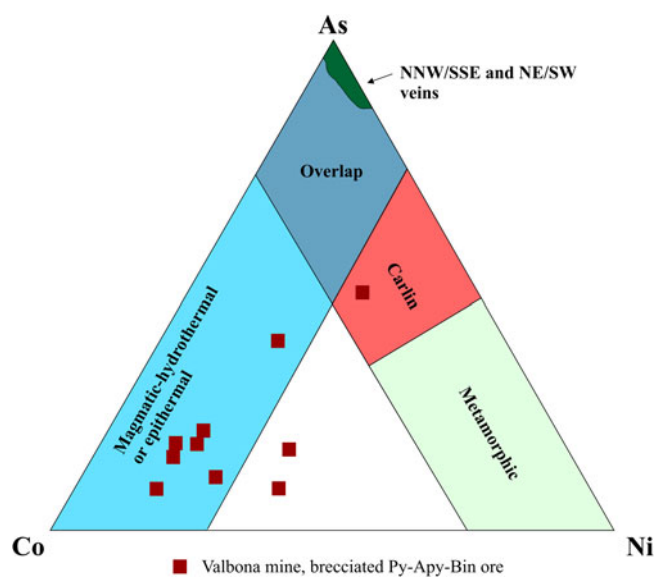


**Figure 12.** Valsassina pyrite compositions compared to other deposits on a Co–Ni–As projection (modified from Rajabpour *et al.*, 2017). The composition of pyrite from the NNW–SSE and NE–SW vein (green area) lies near the As apex, however the brecciated Valbona pyrite data (red squares) is shifted towards the Co apex.

of medium- to low-temperature mineralisation. In more detail, in each of the two vein systems, sphalerite appears to be formed at relatively higher temperatures (up to 190°C) as well as at lower temperatures (as low as 135°C). These observations are consistent with both the minor textural and compositional differences observed in sphalerite from the different veins and the possible multiphase deposition of these veins. Furthermore, by utilising the temperature data obtained from the GGIMFis geothermometer, in conjunction with sulfur concentrations measured using LA–ICP–MS in sphalerite, we were able to plot our data in a sulfur fugacity–temperature diagram (see Fig. 13, adapted from Einaudi *et al.*, 2003). Note that sphalerite samples extracted from both the NNW–SSE and NE–SW vein systems exhibit similar sulfur fugacity values. These values fall within the stability range of pyrite and chalcopyrite, consistent with the observed sulfide assemblages within these veins.

The ore in the Cortabbio lode (Faidallo mine) contains the silver–bismuth sulfide matildite, as exsolution lamellae in galena, with a Widmanstätten-like texture (Fig. 6a). As proposed by Craig (1967), matildite forms a complete solid solution with galena at temperatures above  $215 \pm 15^\circ\text{C}$ , whereas at lower temperatures it exsolves as lamellae in galena. For this reason, matildite exsolution, together with the record of Ag and Bi contents in galena, can be used as a geothermometer for evaluating temperature above, below or near 215°C. In the Cortabbio lode, galena associated with the matildite lamellae always has significant Bi and Ag contents (in wt.% units). Considering the co-association of

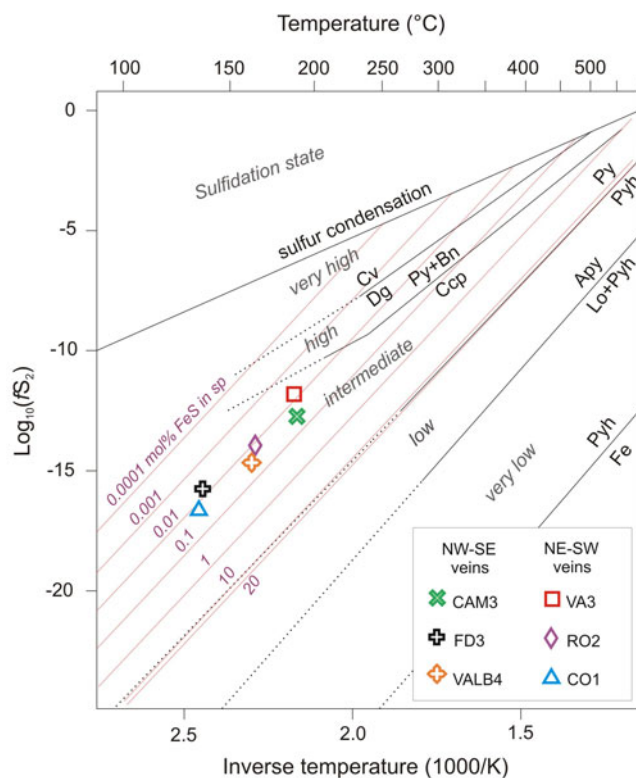


**Figure 13.** Sulfur fugacity/temperature diagram with mineral reaction lines (black) and isolines of Fe concentrations in sphalerite (red). Sphalerites from the NNW–SSE veins and from the NE–SW veins are plotted on the basis of their average % FeS molar contents and of their GGIMFis temperatures. Labels: Apy = arsenopyrite, Bn = bornite, Ccp = chalcopyrite, Cv = covellite, Dg = digenite, Fe = native iron, Lo = löllingite, Po = pyrrhotite, Py = pyrite, Sp = sphalerite. Sample names as in Table 1. Modified after Einaudi *et al.* (2003).

the Ag–Bi-bearing galena and the matildite exsolutions, we can expect that the temperature conditions for the sulfide-rich association of Cortabbio lode are  $\sim 215 \pm 15^\circ\text{C}$ . Note that this estimate is higher compared to the GGIMFis sphalerite geothermometer temperature for the Cortabbio sulfide-rich stage. This observation suggests that galena and bismuth-bearing minerals may form at slightly higher temperatures if compared to the sphalerite-rich assemblage. At Cortabbio, the bismuth minerals represent some of the first precipitated sulfides at the end of the Co–Ni-rich stage. This observation could suggest a slight decrease in deposition temperatures during the sulfide-rich stage at Cortabbio.

Temperature estimations for the Valbona pyrite–arsenopyrite brecciated ore association were obtained by means of the so-called arsenopyrite geothermometer (Kretschmar and Scott, 1976; Sharp *et al.*, 1985): the formation temperature of Valbona pyrite–arsenopyrite-rich ore ranges between 365 and 385°C (see Supplementary Fig. S3 and Table S3b). As discussed above, this distinctive arsenopyrite-rich association probably predates the other sulfides within the Valbona vein. Given this, it is conceivable that the arsenopyrite facies might be related to an older mineralisation, subsequently tectonised by fault reactivation and overprinted by the Valsassina hydrothermal system. Alternatively, it could be related to an earlier, higher-temperature syn-tectonic facies of the Valbona vein.

#### ***The native metals/Ni–Co–Fe arsenides association of Cortabbio lode: Valsassina as a five-element vein system?***

For the description of a possible genetic model of these veins, it is important to consider the occurrence of hydrothermal Ni–Co phases and, in particular, the (high) concentration of Ni–Co–Fe arsenides in the Cortabbio ore. The Valsassina deposits have some of the distinctive features of the so called ‘five-element veins’. In particular, the paragenetic scheme for the Cortabbio vein system is closely comparable with that observed in mining districts for five-element veins worldwide (Fig. 7).

Generally, hydrothermal vein deposits with native Ag, As or Bi overgrown by a succession of Ni, Co and Fe arsenides, usually encapsulated by carbonate gangue minerals, are called five-element veins (for the Ag, As, Co, Ni and Bi element associations; Kissin, 1992). However, this nomenclature does not correctly describe all sub-types of this mineralisation type, as some elements do not occur at some sites and/or elements such as Sb and U can additionally occur in other sites, hence sub-types might be considered. Markl *et al.* (2016), for example, distinguished between native Ag/Bi-dominating, arsenide-dominating and native As-dominating five-element veins. The host-rock composition is also very variable and includes sedimentary, metamorphic and igneous rocks, the latter with felsic to ultramafic composition. Reported formation temperatures, for the contexts where five-element veins occur, range from  $\sim 150$  to  $450^\circ\text{C}$ , though usually cluster at  $\sim 200^\circ\text{C}$  (Kissin, 1992; Staude *et al.*, 2012 – and references therein). According to petrographic observations (e.g. Ramdohr, 1975; Kissin, 1992; Ahmed *et al.*, 2009; Kreissl *et al.*, 2018 and references therein), all the five-element veins can be classified into several (usually four) successive ore stages that may not be observable or accessible in all the sites: ‘Ore stage 1’: sulfides older than native metals and arsenides; ‘Ore stage 2’: native metals; ‘Ore stage 3’: arsenides growing on native metals; and ‘Ore stage 4’: sulfides younger than native metals and arsenides.

The arsenide stage (Ore stage 3) is always followed by base metal sulfides and sulfosalts, such as galena, chalcopyrite, sphalerite and tennantite–tetrahedrite, occasionally accompanied by bismuthinite, acanthite, proustite, pearceite, aikinite, pyrite and others (Ore stage 4). Ore stage 4 is usually followed by a late stage, characterised by precipitation of gangue minerals, usually carbonates, though also baryte in minor cases (Kissin, 1992). Based on textural evidence, Markl *et al.* (2016) assumed a rapid and continuous ore precipitation process in stage 1, 2 and 3, presumably caused by far-from-equilibrium conditions and developing within small fluctuations of the temperature ranges observed among stages in all ore districts. Kissin (1988) suggested that the formation of five-element veins is linked to the circulation of basinal brines during extensional tectonics. Marshall *et al.* (1993) hypothesised that silver deposition is caused by a decrease of chlorine activity as a consequence of the mixing of silver-rich highly saline fluids with connate-meteoric fluids. Recently, Markl *et al.* (2016) suggested that the genesis of these deposits can be ascribed to the mixing between hydrocarbon-bearing fluids and metal-rich hydrothermal fluids, which lead to the formation of the unusual ore textures and assemblages. For example, the hydrocarbon-rich fluids can be the effect of natural fracking phenomena: ejection of hydrocarbons or hydrocarbon-bearing fluids during the breaking up of rocks. Oxidation of methane leads to very reducing conditions for the mixed ore fluid, which facilitates the precipitation of the native metals and arsenides far-from-equilibrium. Moreover, the progressive oxidation of methane leads to precipitation of calcite and other carbonates instead of other gangue minerals like quartz, as a consequence of the dissolution of  $\text{CO}_2$  and concomitant increase in  $\text{HCO}_3^-$  activity. Eventually, the native metals/Ni–Co minerals precipitation stops when the hydrothermal system retains its original equilibrium.

When considering the Valsassina deposits, the Cortabbio vein system has characteristics expected for arsenide-dominated five-element veins and displays features of the ore stages 2, 3 and 4, with both cockade-like textures of the Ni–Co–As enrichments as well as the sulfide-dominating Ore stage 4 particularly well developed. Considering the petrographic features of the Cortabbio vein ore, the Ni–Co arsenides appear to predate the sulfide-rich assemblages. Considering the arsenides, the first precipitated phases are dominated by Ni and represented by mono-arsenide nickeline followed by Co-bearing diarsenide rammeisbergite, followed by Ni–Co sulfarsenides (Fig. 14). Native metals (bismuth, lead and antimony) occur as small inclusions inside the Ni–Co arsenides. The Ni–Co–Fe nodules are always associated with and/or encapsulated in carbonate gangue (mainly siderite and dolomite), therefore they appear mainly as floaters in the carbonate gangue, with no or only very limited contact with the host rock. As stated above, the subsequent As-bearing phases are represented by Ni–Co sulfarsenides, which record the progressive increase of both S and Co in the mineralising fluid: Co-bearing gersdorffite and intermediate members of gersdorffite–cobaltite series crystallise, followed by alloclase and glaucodot (Fig. 14). The latter sulfarsenides are common accessory phases in the Cortabbio samples, rich in sulfides and tetrahedrite, where a bismuth imprint is also well expressed.

In five-element veins, the native elements are usually partly dissolved during or after the growth of the arsenides and sulfarsenides/antimonides, leaving empty holes rimmed by the arsenide minerals (Markl *et al.*, 2016) usually filled by carbonate gangue minerals. In the Cortabbio ore, the nickeline rosettes that

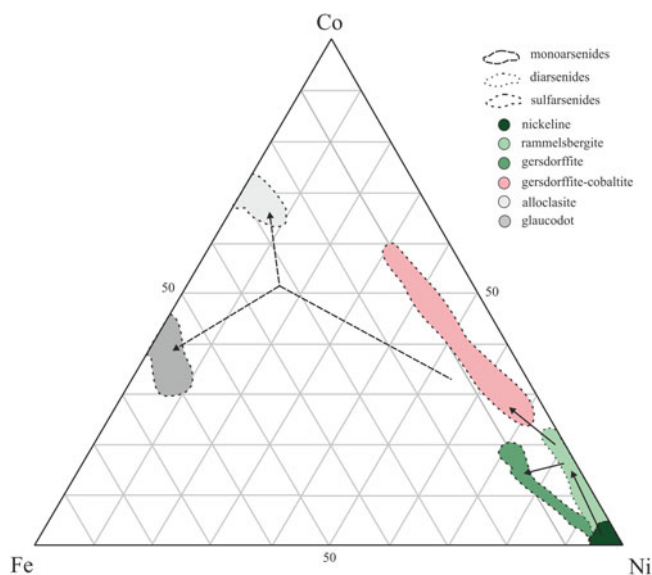


**Figure 14.** Ternary diagram illustrating the composition of the Cortabbio Ni-Co-Fe arsenide and sulfarsenides for evaluation of the chemical trends in the precipitation sequence of these minerals (based on petrographic observations) and for comparing these with observations of five-element veins worldwide. The first crystallised phases have Ni-only or Ni-rich compositions (e.g. nickeline and, partly, rammelsbergite), whereas the minerals deposited subsequently have gradual compositional variations, with moderate and progressive enrichments in Co, followed by Co and Fe, coupled with an increase in As (from mono- to diarsenide) and subsequent input of sulfur (sulfarsenides).

represent the core of the Ni-Co-Fe nodules usually start growing from carbonate fragments. The nickeline mosaic textures suggest that this mineral might have been grown at the expense of another phase (Fig. 5h,i). The gersdorffite-cobaltite crusts, in the external portions of the Ni-Co-Fe nodules, commonly include extremely fine grained, sub-micrometric segregations of native bismuth. This suggests that the Ni-Co arsenide and sulfarsenide also grew after the native bismuth or other native metals. Therefore, the following mineral precipitation sequence can be inferred (see also Fig. 7): (1) native metals; (2) nickeline + rammelsbergite + gersdorffite-cobaltite; and (3) alloclasite-glaucodot + Ag-Bi-Pb sulfide/sulfosalts (galena, aikinite, matildite, wittichenite and ourayite) + chalcopryrite, tennantite, sphalerite, pyrite and bournonite.

Cortabbio may not be the only arsenide-rich vein deposit of the Valsassina district, as preliminary inspection of the poorly accessible Camisolo vein deposit reveals many analogies with Cortabbio. Ni-rich skutterudite nodules were observed in quartz-carbonate veinlets, within hydrothermally altered host volcanics. Remarkably, various arsenates of Co, Ni, U, Bi and heavy REE are associated with this mineralisation (Vergani, 2019; Vergani *et al.*, 2020). In the polymetallic Valbona, rich in sphalerite and Ag-bearing tetrahedrite, and Cobio orebodies (NNW-SSE trending veins), the ore mineral assemblage is comparable with the sulfide-rich association observed at Cortabbio.

The estimated temperatures for the Valsassina vein deposits are comparable with the characteristic temperature ranges measured by fluid-inclusion analyses and reported in the relevant literature for the five-element vein districts.

The two different vein families are possibly genetically related and the base metal rich NE-SW veins might be Ore stage 4 of the five-elements hydrothermal circulation, as well as the sulfide-rich associations of NNW-SSE veins.

The brecciated pyrite-arsenopyrite-rich ore of the Valbona vein is probably attributable to a previous hydrothermal event. At present, there is no direct or clear evidence of the connection of this ore with the other base metal sulfide veins, probably because of the poorly accessible old mine galleries, although there are remarkable similarities between the mineral assemblages (pyrite, chalcopryrite, presence of abundant As as well as accessory Bi phases). The temperature estimation (365–385°C, Fig. 13) for this particular ore association obtained by means of the arsenopyrite geothermometer are higher than the ranges of temperature obtained with the GGIMFis geothermometer for the sulfide-rich stage of Valsassina veins. The Valbona pyrite-arsenopyrite brecciated ore is also characterised by different trace-element concentrations and Co/Ni ratios compared to the Valsassina NNW-SSE and NE-SW veins. In addition, considering the temperature range obtained for this brecciated ore, it is possible to hypothesise an origin potentially ascribed to the hydrothermal circuit of Val Biandino intrusive or to the Permian volcanism. This particular mineralisation might represent Ore stage 1 of the Valsassina hydrothermal system, although with the present data it is not currently possible to fully validate this hypothesis.

In some cases (e.g. Odenwald, Burisch *et al.*, 2017), the five-element veins occur in spatial association with intrusive bodies, however several lines of evidence suggest that mineralisation is unrelated to magmatism. In the case of the Valsassina veins, the timing of the supposed five-element vein system is uncertain although it may have developed after the emplacement of the Val Biandino-Valle San Biagio plutonic complex.

Five-element vein systems are also found in other areas of the Alps, for example Usseglio in Piedmont and Kaltenberg in Switzerland. The veins at Usseglio are hosted in an ophiolite setting within the Western Alpine belt. Within these veins, Ni-Co-Fe arsenides mineralisation precipitated at temperatures of ~170°C, as indicated by fluid-inclusion studies (Moroni *et al.*, 2019a). Interestingly, this mineralisation is not uniformly distributed within the vein system, similar to observations in Valsassina. In fact, Ni-Co-Fe minerals are predominantly found in specific veins, particularly in the eastern portion of the vein swarm. The larger ore lodes are characterised mainly by siderite, together with baryte, ankerite and accessory sulfides. Four distinct ore stages have been identified: (1) siderite, (2) baryte, (3) Co-Ni-Fe arsenides, and finally (4) sulfides (Moroni *et al.*, 2019a). These veins are probably associated with a low-temperature post-orogenic (post-Alpine) hydrothermal circulation of basinal brines, along fractures linked to distensive tectonics (Moroni *et al.*, 2019a).

Similar five-element veins are also found in Kaltenberg, Switzerland, within the metamorphic basement of the Western Alps, Penninic Domain (Kreissl *et al.*, 2018). These veins exhibit a complex geology with two main hydrothermal events (233 ± 10 Ma and 188 ± 32 Ma), related to distensive tectonics during the breakup of the Meliata ocean and Alpine Tethys. These events are also associated with *in situ* remobilisation of ores that occurred during the Alpine Orogeny. In these veins, both Co-rich and Ni-Co-rich assemblages can be identified.

Compared to the Usseglio and Kaltenberg deposits, the Valsassina veins are distinctly Ni-dominated, featuring arsenides and sulfarsenides such as rammelsbergite, nickeline and gersdorffite, with only minor Co-bearing gersdorffite, cobaltite and alloclasite-glaucodot. Additionally, arsenides such as löllingite, safflorite and skutterudite are nearly absent in the Valsassina veins, in contrast to observations at Usseglio and Kaltenberg. In

Valsassina, as well as in other Alpine five-element deposits like Usseglio and Kaltenberg, native Ag is not observable, and the native metals appear to be represented mainly by native Bi, with the addition of native As at Usseglio.

### C and O isotopic signatures of carbonates and fluids

The carbon and oxygen isotope analyses of the carbonate gangue, from the polymetallic and the base metal sulfide veins, provide additional clues to the evaluation of Valsassina deposits. In Fig. 10, additional data, included for comparison, represent the isotopic signatures of marine carbonates of Phanerozoic age, and of carbonates (siderite, dolomite and calcite) from several worldwide Ni–Co bearing, five-element-vein-type mining districts, i.e. Bou Azzer (Morocco; dolomite and calcite, Maacha *et al.*, 2015), Odenwald (SW Germany; calcite, Burisch *et al.*, 2017), Cobalt-Gowganda, Thunder Bay and Great Bear Lake (Canada; Robinson and Badham, 1974, Changkakoti *et al.*, 1986; Kerrich *et al.*, 1986; Kissin, 1992) as well as the Ni–Co-rich Arburese vein system in SW Sardinia (Moroni *et al.*, 2019b). The background also includes isotopic data of sulfide-bearing siderite-bearing late–post Variscan hydrothermal deposits in the Southern Alps (Corтеcci and Frizzo, 1993; Martin *et al.*, 2017), as well as the data from the Variscan syn-orogenic siderite veins of the Siegerland district, Rhenish Massif (Hein, 1993), for which crosscutting relationships with syn-late-orogenic Co–Ni mineralisation were recently recognised (Hellmann *et al.*, 2012). In Fig. 10b, the range of  $\delta^{13}\text{C}$  values from the Valsassina veins are plotted together with an additional literature dataset for five element vein-type districts worldwide: Schwarzwald (SW Germany, Staudе *et al.*, 2007); Kongsberg (Norway; Segalstad *et al.*, 1986; Kissin, 1992); and Great Bear Lake (Canada), with the distinction between isotopic signatures of ore-related dolomite and calcite. The data obtained for the Valsassina veins reveals similarities between: (1) carbonates of the Ni–Co-rich polymetallic veins and of the Ni–Co-poor base metal sulfide veins; and (2) the isotopic signatures of the siderite- and the dolomite-dominated samples. The reference data plotted in Fig. 10a for various worldwide five element vein-type ore districts represent isotope signatures of different carbonates (dolomite, calcite and siderite) and of some different ore stages. The patterns of such reference data appear to be quite variable and, at least in some cases, they reflect fluid evolution or fluctuations in physical–chemical parameters during multistage ore deposition. However, at least one feature is common to all ore districts, as well as to the Valsassina data: the mildly to moderately negative  $\delta^{13}\text{C}$  signatures of ore-related carbonates. There is a large variability in  $\delta^{13}\text{C}$  values in several ore districts, although there is a compositional range of overlap encompassing the  $\delta^{13}\text{C}$  range of the Valsassina veins (Fig. 10a,b). The rather restricted Valsassina data overlaps the compositional fields of the Great Bear Lake ores, of the Sardinian Arburese veins and the narrow field of the ophiolite-hosted Bou Azzer district. There is also similarity between the Valsassina signatures and those belonging to the other Southern Alpine siderite–sulfide ores. The similarity between dolomite and siderite signatures for both carbon and oxygen appears to be a distinctive feature of the Valsassina veins. The overall range of variation in  $\delta^{18}\text{O}$  of the Valsassina samples (from +13.6 to +18.5 *per mil*) is rather pronounced, however it derives from the overlap between the siderite and dolomite compositions (Supplementary Table S4). In the Variscan Siegerland siderite veins, Hein (1993) correlated the

$\delta^{18}\text{O}$  data systematically with variations in trapping temperatures from fluid-inclusion analyses (see Fig. 10a).

An evaluation was done of the oxygen isotopic composition of the fluids in equilibrium with both siderite and dolomite through experimentally determined mineral–water fractionation equations by Zheng (1999) (see section on C and O isotope data above). Fig. 11 displays the plots of the  $\delta^{18}\text{O}$  composition of fluids in equilibrium with siderite and dolomite belonging to the different assemblages (i.e. polymetallic and base metal veins) vs. temperature, according to the method in Mondillo *et al.* (2018). The mineral–fluid fractionation curves for Valsassina siderite and dolomite form bundles displaying moderate overlap across the whole temperature interval shown, from 0° to 400°C (Fig. 11a). However, the plot of the arithmetic averages of the fractionation curves for each group (Fig. 11b) allows us to observe an intersection between the dolomite fractionation curve and the one related to siderite from polymetallic veins. The low-angle intersection involves a wide temperature interval, spanning from approximately 50° to 125°C; however, the upper range of such interval is compatible with the lower temperature estimates obtained by means of the sphalerite geothermometer for polymetallic veins (130–140°C; see Estimation of the temperatures of ore formation, above and Fig. 13).

In addition to confirming the overall isotopic coherence among the Valsassina hydrothermal veins, these observations suggest that the dolomite-bearing base metal veins, poorly exposed in some of the old Valsassina mining sites, might be related to the main mineralised system represented by the polymetallic veins and represent peripheral portions of such a system.

For the siderite veins for which a thermometric estimate from sphalerite is available (Cortabbio, Valbona, Valtorta and Rossiga), it was possible to estimate the  $\delta^{13}\text{C}$  composition of the fluid in equilibrium with siderite, for the temperature ranges of 130–140° and 160–190°C, using the equation given by Golyshev *et al.* (1981) (see C and O isotope data, above). The corresponding equation for dolomite–fluid fractionation by Golyshev *et al.* (1981) was employed to estimate the isotopic  $\delta^{13}\text{C}$  signature of the fluid in equilibrium with the average dolomite  $\delta^{13}\text{C}$  composition at 120–130°C, i.e. near the upper limit of the overlap between the fluid fractionation curves for siderite and dolomite in Fig. 11b. All fluid  $\delta^{13}\text{C}$  signatures for siderite and dolomite are negative, between –6.8 and –13 *per mil* (see Supplementary Table S4), only marginally intersecting the restricted range of the igneous carbon reservoir ( $\delta^{13}\text{C} = -4$  to  $-7$  *per mil*; Hoefs, 2009). These results suggest that the siderite- and dolomite-bearing ores might have crystallised from broadly similar fluids, although the lighter  $\delta^{13}\text{C}$  fluid values, recorded in siderite samples, might be the result of interaction with organic carbon-bearing rocks.

### Age and metal sources

Direct intersections between the base metal and five-element/polymetallic veins are not observable, neither in the accessible mining works nor in the outcrops. The most recent information available for the fault systems that host the orebodies is restricted to the work by Pohl *et al.* (2018, and references therein), who support the early Permian age of some of the structures in relation to N–S extensional tectonics, and a modest reactivation during the Alpine orogeny. Geochronological data of the mineralised bodies in Valsassina are currently not available; however, a late–post Variscan age may be viable in response to the observed

crosscutting relationships and the evaluations by Pohl *et al.* (2018). In fact, these veins crosscut the Valsassina plutons and are truncated by the erosional unconformity at base of the Verrucano Lombardo Fm. (Bianchi, 1999), suggesting a vein emplacement between Lower and Upper Permian. This age estimation is also comparable with the time span of the regional-scale siderite  $\pm$  polymetallic sulfide mineralisation that affected large sectors of the Southern Alpine domain (Martin *et al.*, 2017). These siderite  $\pm$  sulfide veins are also evident in Valsassina, and are frequently found near the areas characterised by the sulfide veins discussed in this study. The genesis of the siderite  $\pm$  sulfide veins is probably linked to a hydrothermal circulation of iron-rich fluids during the Permian to Early Triassic period, characterised by groundwater originating from meteoric freshwater (also with a marine contribution during the Early Triassic) infiltrated along syn-depositional faults, and heated up to 250°C at depths of 1000–2000 metres by the high geothermal gradient due to the Permian magmatism. In these veins, minerals such as galena and sphalerite are usually present as accessory sulfides, which, in contrast, dominate in the Valsassina veins. The sulfide associations in the Valsassina veins are notably more similar to those documented in the quartz breccias of the Gromo-Gandellino area, characterised by galena, sphalerite, chalcopyrite, pyrite, arsenopyrite and tetrahedrite (Servida *et al.*, 2010). The genesis of these quartz–sulfide breccias is associated with a hydrothermal circuit connected to volcano–phreatic activity; in fact, the breccia bodies can be the product of early phreato–magmatic activity related to the volcanism of the Collio Basin (Servida *et al.*, 2010). In both the sulfide-bearing breccias and the siderite  $\pm$  sulfide veins, Ni–Co sulfarsenides can be recognised as accessory phases, although the occurrence of Ni–Co mineralisation ascribable to five-element vein-type deposits makes the Valsassina vein system different from the other late Variscan Southern Alpine hydrothermal systems.

As discussed above, the arsenide-free and probably granite-related pyrite–arsenopyrite-rich brecciated Valbona mineralisation might be considered as a potential Ore stage 1. If so, the local magmatic rocks may have played a role on the presence of Ni and Co in the five-element vein mineralisation. Nickel and Co in these veins might have been leached by the hydrothermal fluids from the basic portions of the Val Biandino intrusive complex, or from the amphibolite horizons widespread in the Orobic basement (Cadel *et al.*, 1996; De Sitter and De Sitter-Koomans, 1949). However, the potential of mafic rocks alone for Co mineralisation has been discussed recently by Konnunaho *et al.* (2018), who envisaged the necessity of contamination processes of mafic rocks, especially through post-magmatic hydrothermal alteration and pre-enrichment of metals, in particular Co, by influx of CO<sub>2</sub>-rich saline fluids. These saline fluids are not far from those considered in the model outlined by Kissin (1988; 1992), who suggested that the formation of five-element veins is caused by the circulation of connate brines ('basinal brines') in environments of continental rifting, i.e. in the same tectonic regime that characterised the Southern Alps during the Permian–Early Triassic. In contrast, considering instead the model proposed by Markl *et al.* (2016), the Valsassina veins might be the effect of the small-scale interaction between hydrocarbon-rich fluids and a pre-existing hydrothermal system, probably not too dissimilar from those already described in other areas of the Southern Alps associated with late–post Variscan tectonic–magmatic activity. The hydrocarbon sources can be ascribed to the graphite schist and black-shale levels in

the metamorphic basement and in the Collio Formation, respectively.

No data are available for the fluids responsible for the extensive vein system developed in Valsassina. In this light, it is currently not possible to correlate the veins to a plumbing system alimented by basinal brines, similar to those recorded in the other five element vein-type deposits or to interaction with hydrocarbon-rich fluids.

## Conclusions

The sulfide veins in the Valsassina region have not previously received any comprehensive studies, with research being largely of a fragmented character. The present work represents an initial effort to provide a more detailed overview of these sulfide-bearing veins. However, due to challenges in sampling arising from the status of old mining works and the lack of supplementary data such as fluid-inclusion studies, it is essential to regard this work as preliminary. Nevertheless, it has enabled us to gain a more in-depth understanding of these veins, which exhibit characteristics typical of five-element veins, especially in the case of the Cortabbio lode.

Field studies and petrographic observations have revealed the presence of two distinct vein families. One is polymetallic and NNW–SSE oriented, whereas the other is NE–SW oriented and primarily characterised by base metal sulfides, with sulfosalts and nickel–cobalt sulfoarsenides present as accessory phases. Petrographic analysis revealed no significant differences in ore mineral textures between the two veins families. Instead, the distinction between the families seems to be based primarily on the different relative concentrations of metallic minerals. Trace-element studies of pyrite have found no substantial differences between the two vein families. In contrast, trace-element studies of sphalerite indicated some variations in indium and iron contents. These differences are also reflected in the slightly different temperature estimates obtained using the Frenzel *et al.* (2017) geothermometer for these veins. The C and O stable-isotope data obtained for the Valsassina veins reveals similarities between carbonates of the Ni–Co-rich polymetallic veins and of the Ni–Co-poor base metal sulfide veins, as well as the isotopic signatures of the siderite- and the dolomite-dominated samples.

On the basis of the data obtained, it is conceivable that the NNW–SSE veins might represent Ore stage 4 of the five-element system. The NE–SW veins could be associated with either stage 4 or, alternatively, might represent Ore stage 1 of the five-element system. At present, direct intersections between the base metal and five-element/polymetallic veins have not been observed, neither in accessible mining operations nor in outcrops. Therefore, the relationship between the two vein systems remains unclear, and the current data does not allow us to validate either of these hypotheses.

Geochronological data for the mineralised bodies in Valsassina are currently not available, however a late–post Variscan age may be viable on the basis of the observed cross-cutting relationships and the evaluations by Pohl *et al.* (2018). This age estimation would also be comparable with the time span of the regional-scale siderite  $\pm$  polymetallic sulfide mineralisation affecting large sectors of the Southern Alpine domain (Martin *et al.*, 2017), although the occurrence of Ni–Co mineralisation, ascribable to five-element vein-type deposits, distinguishes the Valsassina vein system from the other Southern Alpine siderite–sulfide vein systems.

**Acknowledgements.** G. Diego Gatta and Marilena Moroni acknowledge the support of the Italian Ministry of Education (MUR) through the projects “Dipartimenti di Eccellenza 2023–2027” and “PRIN2017 - Mineral reactivity, a key to understand large-scale processes” (2017-L83S77). The authors are indebted to Dr. Elena Ferrari (ESD-MI) for the assistance during the stable isotope analyses and to Mr. Fabio Marchesini (ESD-MI) and Mr. Andrea Risplendente (UNITECH COSPECT – MI) in samples preparation and assistance for the EMPA–WDS analysis. Fabrizio Vergani is grateful to Luigi Possenti and Giancarlo Valsecchi, mineral collectors and great connoisseurs of the mining history of Valsassina, for the information on the studied localities and for various samples, and to Massimiliano Stucchi, Andrea Gnata and Monica Corti for the help during the field works. The Editors and two anonymous Reviewers are thanked for the revision of the manuscript. This manuscript is dedicated to the memory of our friend and colleague Dr. Alessandro Guastoni, who worked extensively in Valsassina.

**Competing interests.** The authors declare none

**Supplementary material.** The supplementary material for this article can be found at <https://doi.org/10.1180/mgm.2024.3>.

## References

- Ahmed A.H., Arai S. and Ikenne M. (2009) Mineralogy and paragenesis of the Co-Ni arsenide ores of Bou Azzer, Anti-Atlas, Morocco. *Economic Geology*, **104**, 249–266.
- Artini E. (1903) Note mineralogiche sulla Valsassina. *Atti della Società Italiana di Scienze Naturali*, **42**, 1–19.
- Beaudoin G. and Therrien P. (2009) The updated web stable isotope fractionation calculator. Pp. 1120–1122 in: *Handbook of Stable Isotope Analytical Techniques* (P.A. De Groot, editor). Elsevier, Netherland.
- Belissant R., Boiron M.C., Luais B. and Cathelineau M. (2014) LA-ICPMS analyses of minor and trace elements and bulk Ge isotopes in zoned Ge-rich sphalerites from the Noailhac–Saint-Salvy deposit (France): Insights into incorporation mechanisms and ore deposition processes. *Geochimica et Cosmochimica Acta*, **126**, 518–540.
- Berra F. and Siletto G.B. (2006) Controllo litologico e stratigrafico sull’assetto strutturale delle Alpi meridionali lombarde: il ruolo degli orizzonti di scollamento. *Rendiconti della Società Geologica Italiana Nuova Serie*, **1**, 1–3.
- Berra F., Felletti F. and Tessarollo A. (2016) Stratigraphic architecture of a transtensional continental basin in low-latitude semiarid conditions: The Permian succession of the Central Orobic Basin (Southern Alps, Italy). *Journal of Sedimentary Research*, **86**, 408–429.
- Bianchi A. (1999) *Mineralizzazioni a barite e solfuri di Pb, Zn, Cu, Fe e Ag nel basamento cristallino della media Valsassina (LC)*. Master thesis dissertation, University of Milan, Italy.
- Bralia A., Sabatini G. and Troja F. (1979) A reevaluation of the Co/Ni ratio in pyrite as geochemical tool in ore genesis problems. *Mineralium Deposita*, **14**, 353–374.
- Burisch M., Gerdes A., Walter B. F., Neumann U., Fettel M. and Markl G. (2017) Methane and the origin of five-element veins: Mineralogy, age, fluid inclusion chemistry and ore forming processes in the Odenwald, SW Germany. *Ore Geology Reviews*, **81**, 42–61.
- Cadel G. (1986) Geology and uranium mineralization of the Collio Basin (central Southern Alps, Italy). *Uranium*, **18**, 215–240.
- Cadel G., Cosi M., Pennacchioni G. and Spalla M.I. (1996) A new map of the Permo-Carboniferous cover and Variscan metamorphic basement in the central Orobic Alps, southern Alps, Italy: structural and stratigraphical data. *Memorie di Scienze Geologiche*, **48**, 1–53.
- Changkakoti A., Morton R. D., Gray J. and Yonge C. J. (1986) Oxygen, hydrogen, and carbon isotopic studies of the Great Bear Lake silver deposits, Northwest Territories. *Canadian Journal of Earth Sciences*, **23**, 1463–1469.
- Cook N.J. and Chryssoulis S.L. (1990) Concentrations of “invisible gold” in the common sulfides. *The Canadian Mineralogist*, **28**, 1–16.
- Cook N.J., Ciobanu C.L., Pring A., Skinner W., Shimizu M., Danyushevsky L., Saini-Eidukat B. and Melcher F. (2009a) Trace and minor elements in sphalerite: A LA-ICPMS study. *Geochimica et Cosmochimica Acta*, **73**, 4761–4791.
- Cook N.J., Ciobanu C.L. and Mao J. (2009b) Textural control on gold distribution in As-free pyrite from the Dongping, Huangtuliang and Hougou gold deposits, North China Craton (Hebei Province, China). *Chemical Geology*, **264**, 101–121.
- Cook N.J., Ciobanu C.L., Brugger J., Etschmann B., Howard D.L., De Jonge M.D., Ryan C. and Paterson D. (2012) Determination of the oxidation state of Cu in substituted Cu-In-Fe-bearing sphalerite via  $\mu$ XANES spectroscopy. *American Mineralogist*, **97**, 476–479.
- Cortecchi G. and Frizzo P. (1993) Origin of siderite deposits from the Lombardy Valleys, northern Italy: a carbon, oxygen and strontium isotope study. *Chemical Geology*, **105**, 293–303.
- Craig J.R. (1967) Phase relations and mineral assemblages in the Ag-Bi-Pb-S system. *Mineralium Deposita*, **1**, 278–306.
- Crippa C. (2017) *Relazione tra il magmatismo Permiano e le strutture estensionali: caso di studio del Plutone della Val Biandino (Valsassina, LC)*. Master thesis dissertation, Milano Bicocca University, Italy.
- De Capitani L. (1982) Contributo alla conoscenza dei plutoni sudalpini: le masse intrusive della Val Biandino (Como). *Rendiconti Società Italiana di Mineralogia e Petrologia*, **38**, 109–118.
- De Capitani L. and Liborio G. (1988) Trace element abundance in the Val Biandino Pluton (Southern Alps, Italy). *Memorie della Società di Scienze Geologiche*, **40**, 99–110.
- Deditius A., Utsunomiya S., Ewing R.C. and Kesler S.E. (2009) Nanoscale “liquid” inclusions of As-Fe-S in arsenian pyrite. *American Mineralogist*, **94**, 394.
- Deditius A.P., Reich M., Kesler S.E., Utsunomiya S., Chryssoulis S.L., Walshe J. and Ewing R.C. (2014) The coupled geochemistry of Au and As in pyrite from hydrothermal ore deposits. *Geochimica et Cosmochimica Acta*, **140**, 644–670.
- De Sitter L.U. and De Sitter-Koomans C.M. (1949) Geology of the Bergamasca Alps, Lombardia, Italy. *Leidse Geologische Mededelingen*, **14**, 1–257.
- Di Colbertaldo D. (1967) *Giacimenti minerari*. CEDAM, Milano, Italy, 383 pp.
- Einaudi M., Hedenquist J. and Inan E. (2003) Sulfidation state of fluids in active and extinct hydrothermal systems: Transitions from porphyry to epithermal environments. Pp. 285–313 in: *Volcanic, Geothermal, and Ore-forming Fluids: Rulers and Witnesses of Processes within the Earth* (S. Simmons and I. Graham, editors). Society of Economic Geologists Special Publication, Colorado, USA.
- Frenzel M., Tamino H. and Gutzmer J. (2016) Gallium, germanium, indium, and other trace and minor elements in sphalerite as a function of deposit type — A meta-analysis. *Ore Geology Reviews*, **76**, 52–78.
- Froitzheim N., Derks J. F., Walter J. M. and Sciunnach D. (2008) Evolution of an Early Permian extensional detachment fault from synintrusive, mylonitic flow to brittle faulting (Grassi Detachment Fault, Orobic Anticline, southern Alps, Italy). *Geological Society London*, **298**, 69–82.
- Gaetani M., Sciunnach D., Bini A. and Rossi S. (2012) *Note illustrative della Carta Geologica d’Italia alla scala 1:50.000, F. 076 Lecco*. Progetto CARG, Regione Lombardia, 227 pp.
- Genna D. and Gaboury D. (2015) Deciphering the hydrothermal evolution of a VMS system by LA-ICP-MS using trace elements in pyrite: An example from the Bracemac-Mcleod deposits, Abitibi, Canada, and Implications for Exploration. *Economic Geology*, **110**, 2087–2108.
- Golyshev S.I., Padalko N.L. and Pechenkin S.A. (1981) Fractionation of stable oxygen and carbon isotopes in carbonate systems. *Geochemistry International*, **18**, 85–99.
- Gottesmann W. and Kampe A. (2007) Zn/Cd ratios in calcisilicate-hosted sphalerite ores at Tumurtijn-ovoo, Mongolia. *Chemie der Erde – Geochemistry*, **67**, 323–328.
- Gottesmann W., Gottesmann B. and Seifert W. (2009) Sphalerite composition and ore genesis at the Tumurtijn-ovoo Fe–Mn–Zn skarn deposit, Mongolia. *Neues Jahrbuch für Mineralogie*, **185**, 249–280.
- Guastoni A., Gentile P. and Nestola F. (2015) Aikinite. Cortabbio, Primaluna, Valsassina (LC). *Rivista Mineralogica Italiana*, **39**, 58–61.
- Guastoni A., Gentile P., Nestola F. and Possenti L. (2016a) Baumstarkite di Prapiazzo, Introbio, Valsassina (LC). *Rivista Mineralogica Italiana*, **50**, 120 [abstract].
- Guastoni A., Gentile P., Nestola F. and Possenti L. (2016b) Imiterite di Prapiazzo, Introbio, Valsassina (LC). *Rivista Mineralogica Italiana*, **50**, 120–121 [abstract].



- Hein U.F. (1993) Synmetamorphic Variscan siderite mineralisation of the Rhenish Massif, Central Europe. *Mineralogical Magazine*, **57**, 451–467.
- Hellmann A., Cormann A. and Meyer F.M. (2012) Syn-late orogenic vein hosted Co-Ni mineralization in the Siegerland-District of the Rhenish Massif, NW Germany. *Proceedings of European Mineralogical Conference EMC2012*, **1**, 616.
- Hoefs J. (2009) *Stable Isotope Geochemistry*. Springer, Berlin, 286 pp.
- Kerrich R., Strong D.F., Andrews A.J. and Owsiacki L. (1986) The silver deposits at Cobalt and Gowganda, Ontario. III: Hydrothermal regimes and source reservoirs - evidence from H, O, C and Sr isotopes and fluid inclusions. *Canadian Journal of Earth Sciences*, **23**, 1519–1550.
- Kissin S.A. (1988) Nickel-Cobalt-Native Silver (Five-Element) Veins: A Rift related Ore Type. Pp. 268–279 in: *North American Congress on Tectonic Control of Ore Deposits and the Vertical and Horizontal Extent of Ore Systems*, University of Missouri-Rolla, USA.
- Kissin S.A. (1992) Five-element (Ni–Co–As–Ag–Bi) veins. *Geoscience Canada*, **19**, 113–124.
- Koglin N., Frimmel H.F., Lawrie Minter W.E. and Brätz H. (2010) Trace-element characteristics of different pyrite types in Mesoproterozoic placer deposits. *Mineralium Deposita*, **45**, 259–280.
- Konnunaho J. P., Hanski E., Karinen T. and Lahaye Y. (2018) The petrology and genesis of the Paleoproterozoic mafic intrusion-hosted Co-Cu-Ni deposit at Hietakero, NW Finnish Lapland. *Bulletin of the Geological Society of Finland*, 104–131.
- Kreissl S., Gerdes A., Walter B.F., Neumann U., Wenzel T. and Markl G. (2018) Reconstruction of a >200 Ma multi-stage “five element” Bi-Co-Ni-Fe-As-S system in the Penninic Alps, Switzerland. *Ore Geology Reviews*, **95**, 746–788.
- Kretschmar U. and Scott S.D. (1976) Phase relations involving arsenopyrite in the system Fe-As-S and their application. *The Canadian Mineralogist*, **14**, 364–386.
- Kullerud G. (1953) The FeS-ZnS system, a geological thermometer. *Norsk Geologisk Tidsskrift*, **32**, 62–144.
- Large R.R., Danyushevsky L., Hollit C., Maslennikov V., Meffre S., Gilbert S., Bull S., Scott R., Emsbo P., Thomas H., Singh B. and Foster J. (2009) Gold and trace element zonation in pyrite using a laser imaging technique: implications for the timing of gold in orogenic and Carlin-style sediment-hosted deposits. *Economic Geology*, **104**, 635–668.
- Laubscher H.P. (1985) Large-scale, thin-skinned thrusting in the southern Alps: Kinematic models. *Geological Society of America Bulletin*, **96**, 710–718.
- Li X., Bai L., Yue Z., Pang B. and Wei D. (2021) Mineralization processes involved in the formation of the Jinya Carlin-type Au deposit, northwestern Guangxi, China: Evidence from in situ trace element and S isotope geochemistry of Au-bearing zoned pyrite. *Ore Geology Reviews*, **138**, 104376.
- Locchi S., Zanchetta S. and Zanchi A. (2022) Evidence of Early Permian extension during the post-Variscan evolution of the central Southern Alps (N Italy). *International Journal of Earth Sciences*, **111**, 1717–1738.
- Longerich H.P., Jackson S.E. and Günther D. (1996) Laser ablation inductively coupled plasma mass spectrometric transient signal data acquisition and analyte concentration calculation. *Journal of Analytical Atomic Spectrometry*, **11**, 899–904.
- Maacha L., Lebedev V.I., Saddiqi O., Zouhair M., Elghorfi M., Borissenko A.S. and Pavlova G.G. (2015) *Arsenide Deposits of the Bou Azzer Ore District (Anti-Atlas Metallogenic Province) and their Economic Outlook*. TuvIENR SB RAS Monography, Yarmolyuk, 66 pp.
- Markl G., Burish M. and Neumann U. (2016) Natural fracking and the genesis of five-element veins. *Mineralium Deposita*, **51**, 703–712.
- Marshall D.D., Diamond L.W., and Skippen G.B. (1993) Silver transport and deposition at Cobalt, Ontario, Canada; fluid inclusion evidence. *Economic Geology*, **88**, 837–854.
- Martin S., Toffolo L., Moroni M., Montorfano C., Secco L., Agnini P., Nimis P. and Tumiatì S. (2017) Siderite deposits in northern Italy: Early Permian to Early Triassic hydrothermalism in the Southern Alps. *Lithos*, **285**, 276–295.
- Mondillo N., Herrington R., Boyce A.J., Wilkinson C., Santoro L. and Rumsey M. (2018) Critical elements in non-sulfide Zn deposits: a reanalysis of the Kabwe Zn-Pb ores (central Zambia). *Mineralogical Magazine*, **82**, 89–114.
- Moroni M., Rossetti P., Naitza S., Magnani L., Ruggieri G., Aquino A., Tartarotti P., Franklin A., Ferrari E., and Castelli D. (2019a) Factors controlling hydrothermal nickel and cobalt mineralization – some suggestions from historical ore deposits in Italy. *Minerals*, **9**, 429.
- Moroni M., Naitza S., Ruggieri G., Aquino A., Costagliola P., De Giudici G., Caruso S., Ferrari E., Fiorentini M.E. and Lattanzi P. (2019b) The Pb–Zn–Ag vein system at Montevecchio-Ingurtosu, southwestern Sardinia, Italy: A summary of previous knowledge and new mineralogical, fluid inclusion and isotopic data. *Ore Geology Reviews*, **115**, 103194.
- Pasquarè G. (1967) Analisi geologico-strutturale del complesso intrusivo di Val Biandino (Alpi Orobiche occidentali). *Memorie della Società Geologica Italiana*, **6**, 343–357.
- Paul D., Skrzypek G. and Fórizs I. (2007) Normalization of measured stable isotopic compositions to isotope reference scales – A review. *Rapid Communications in Mass Spectrometry*, **21**, 3006–3014.
- Pohl F., Froitzheim N., Obermüller G., Tomaschek F., Schröder O., Nagel T. J., Sciunnach D. and Heuser A. (2018) Kinematics and age of syn-intrusive detachment faulting in the Southern Alps: Evidence for Early Permian crustal extension and implications for the Pangea A versus B controversy. *Tectonics*, **37**, 3668–3689.
- Price B.G. (1972) *Minor Elements in Pyrites from the Smithers Map Area, B.C. and Exploration Applications of Minor Elements Studies*. PhD dissertation, University of British Columbia, Canada.
- Qian X. (1987) Trace elements in galena and sphalerite and their geochemical significance in distinguishing the genetic types of Pb–Zn ore deposits. *Chinese Journal of Geochemistry*, **6**, 177–190.
- Rajabpour S., Behzadi M., Jiang S.Y., Rasa I., Lehmann B. and Ma Y. (2017) Sulfide chemistry and sulfur isotope characteristics of the Cenozoic volcanic-hosted Kuh-Pang copper deposit, Saveh county, northwestern central Iran. *Ore Geology Reviews*, **86**, 563–583.
- Ramdohr P. (1975) Der Silberkobalterygang mit Kupfererzen vom Wingertsberg bei Nieder-Ramstadt im Odenwald. *Aufschluss*, **27**, 237–243.
- Reich M., Kesler S.E., Utsunomiya S., Palenik C.S., Chryssoulis S.L. and Ewing R.C. (2005) Solubility of gold in arsenian pyrite. *Geochimica et Cosmochimica Acta*, **69**, 2781–2796.
- Reich M., Deditius A., Chryssoulis S., Li J.W., Ma C.Q., Parada M.A., Barra F. and Mittermayr F. (2013) Pyrite as a record of hydrothermal fluid evolution in a porphyry copper system: a SIMS/EMPA trace element study. *Geochimica et Cosmochimica Acta*, **104**, 42–62.
- Robinson B.W. and Badham J.P.N. (1974) Stable isotope geochemistry and the origin of the Great Bear Lake silver deposits, Northwest Territories, Canada. *Canadian Journal of Earth Sciences*, **11**, 698–711.
- Rodeghiero F., Jadoul F., Vailati G. and Venerandi I. (1986) Dati preliminari sulle mineralizzazioni a Pb–Zn dell’area tra Mandello e Ballabio (Lombardia Centrale). *Memorie della Società Geologica Italiana*, **32**, 133–150.
- Schwartz M.O. (2000) Cadmium in zinc deposits: economic geology of a polluting element. *International Geology Review*, **42**, 445–469.
- Sciunnach D. (2001) Early Permian Palaeofaults at the western boundary of the Collio Basin (Valsassina, Lombardy). *Natura Bresciana*, **25**, 37–43.
- Segalstad T.V., Johansen H. and Ohmoto H. (1986) Geochemistry of hydrothermal processes at the Kongsberg silver deposit, southern Norway. *Terra Cognita*, **6**, 511–555.
- Servida D., Moroni M., Ravagnani D., Rodeghiero F., Venerandi I., De Capitani L. and Grieco G. (2010) Phreatic sulphide bearing quartz breccias between crystalline basement and Collio formation (Southern Alps, Italy). *Italian Journal of Geosciences*, **129**, 223–236.
- Sharp Z.D., Essene E.J. and Kelly W.C. (1985) A re-examination of the arsenopyrite geothermometer: pressure considerations and applications to natural assemblages. *The Canadian Mineralogist*, **23**, 517–534.
- Siletto G.B., Spalla M.L., Tunesi A., Lardeaux J.M. and Colombo A. (1993) Pre-Alpine structural and metamorphic histories in the Orobic Southern Alps, Italy. *Pre-Mesozoic Geology in the Alps*, 585–598.
- Staupe S., Wagner T. and Markl G. (2007) Mineralogy, mineral compositions and fluid evolution at the Wenzel hydrothermal deposit, Southern Germany: implications for the formation of Kongsberg-type silver deposits. *The Canadian Mineralogist*, **45**, 1147–1176, doi:10.2113/gscanmin.45.5.1147
- Staupe S., Werner W., Mordhorst T., Wemmer K., Jacob D.E. and Markl G. (2012) Multi-stage Ag–Bi–Co–Ni–U and Cu–Bi vein mineralization at Wittichen, Schwarzwald, SW Germany: geological setting, ore mineralogy, and fluid evolution. *Mineralium Deposita*, **47**, 251–276.

- Tizzoni M. (1998) *Il comprensorio minerario e metallurgico valsassinese*. Monografie Museo Civico Lecco, Lecco, 447 pp.
- Vergani F. (2019) *Le mineralizzazioni filoniane a solfuri della Valsassina: studio giacimentologico preliminare*. Master thesis dissertation, University of Milano, Italy.
- Vergani F. (2022) A preliminary petrographic and LA-ICP-MS trace elements study of the iron sulfide-rich deposits of Lombard Southern Alps: evidences of a hydrothermal origin? *Periodico di Mineralogia*, **91**, 201–224.
- Vergani F., Gentile P., Guastoni A., and Possenti L. (2020) La mineralizzazione ad arseniati e i minerali di antimonio di Passo Camisolo, Introbio (LC) e Valtorta (BG). *Rivista Mineralogica Italiana*, **44**, 44–62.
- Wang C.M., Yang L., Bagas L., Evans N.J., Chen J. and Du B. (2018) Mineralization processes at the giant Jinding Zn-Pb deposit, Lanping Basin, Sanjiang Tethys Orogen: evidence from in situ trace element analysis of pyrite and marcasite. *Geological Journal*, **53**, 1279–1294.
- Warr L.N. (2021) IMA–CNMNC approved mineral symbols. *Mineralogical Magazine*, **85**, 291–320.
- Ye L., Cook N.J., Ciobanu C.L., Liu Y.P., Zhang Q., Liu T.G., Gao W., Yang Y.L. and Danyushevskiy L. (2011) Trace and minor elements in sphalerite from base metal deposits in South China: a LA-ICPMS study. *Ore Geology Review*, **39**, 188–217.
- Zanchetta S., Malusà M.G. and Zanchi A. (2015) Precollisional development and Cenozoic evolution of the Southalpine retrobelt (European Alps). *Lithosphere*, **7**, 662–681.
- Zanchetta S., Locchi S., Carminati G., Mancuso M., Montemagni C. and Zanchi A. (2022) Metasomatism by boron-rich fluids along Permian low-angle normal faults (Central Southern Alps, N Italy). *Minerals*, **12**, 404.
- Zheng Y.F. (1999) Oxygen isotope fractionation in carbonate and sulfate minerals. *Geochemical Journal*, **33**, 2, 109–126.